


Article

Tectonic Generation of Pseudotachylytes and Volcanic Rocks: Deep-Seated Magma Sources of Crust-Mantle Transition in the Baikal Rift System, Southern Siberia

Sergei Rasskazov ^{1,2,*}, Irina Chuvashova ^{1,2}, Tatyana Yasnygina ¹ , Elena Saranina ^{1,3}, Nikolay Gerasimov ³, Youseph Ailow ^{1,4} and Yi-Min Sun ⁵

- ¹ Institute of the Earth's Crust, Siberian Branch of Russian Academy of Sciences, 664033 Irkutsk, Russia; chuvashova@crust.irk.ru (I.C.); ty@crust.irk.ru (T.Y.); e_v_sar@mail.ru (E.S.); youseph.gh.g@gmail.com (Y.A.)
- ² Geological faculty, Irkutsk State University, 664003 Irkutsk, Russia
- ³ Vinogradov Institute of Geochemistry, Siberian Branch of Russian Academy of Sciences, 664033 Irkutsk, Russia; sdril@igc.irk.ru
- ⁴ Faculty of Science, Al-Furat University, Deir ez-Zor, Syria
- ⁵ Institute of Natural Resources and Ecology, Heilongjiang Academy of Science, Harbin 164155, China; sunyimin1988@gmail.com
- * Correspondence: rasskaz@crust.irk.ru; Tel.: +7-3952-511659

Abstract: Volcanic rocks from deep-seated sources of the crust-mantle transition (CMT) are geochemically distinguished from those of ocean island basalts (OIB). Here, we report geochemical data on tectonic pseudotachylytes from the Main Sayan Fault (MSF) and volcanic rocks from the Kamar-Stanovoy Zone of Hot Transtension (KSZHT) that represent the deep-seated CMT magmatic sources in the central part of the Baikal Rift System (BRS). The tectonic generation of the KSZHT magmas between 18.1 and 11.7 Ma is compared with present-day seismogenic deformations in the middle-upper crust of the South Baikal Basin and adjacent Tunka Valley, where strong earthquakes are distributed along the Main Sayan and Primorye sutures of the Siberian paleocontinent. From a detail seismic tomography model and geological evidence, we infer that the KSZHT crust-mantle magmatic processes were due to delamination and lamination of a thickened root part of the South Baikal Orogen existed in the Late Cretaceous and Paleogene. In addition, we identify similar deep-seated CMT sources for melts erupted in the past 17 Ma from a delaminated root part of the East Hangay Orogen and adjacent Orkhon-Selenga Saddle in the southwestern BRS. We suggest that both in the central and in the southwestern BRS, the deep-seated CMT magma sources designate cooperative pull-to-axis and convergent effects created in the Japan-Baikal Geodynamic Corridor and in the Indo-Asian interactional region, respectively.

Keywords: pseudotachylytes; volcanic rocks; Cenozoic; crust-mantle boundary; Baikal Rift System; Southern Siberia



Citation: Rasskazov, S.; Chuvashova, I.; Yasnygina, T.; Saranina, E.; Gerasimov, N.; Ailow, Y.; Sun, Y.-M. Tectonic Generation of Pseudotachylytes and Volcanic Rocks: Deep-Seated Magma Sources of Crust-Mantle Transition in the Baikal Rift System, Southern Siberia. *Minerals* **2021**, *11*, 487. <https://doi.org/10.3390/min11050487>

Academic Editor: Shoji Arai

Received: 18 March 2021

Accepted: 30 April 2021

Published: 2 May 2021

Publisher's Note: MDPI stays neutral with regard to jurisdictional claims in published maps and institutional affiliations.



Copyright: © 2021 by the authors. Licensee MDPI, Basel, Switzerland. This article is an open access article distributed under the terms and conditions of the Creative Commons Attribution (CC BY) license (<https://creativecommons.org/licenses/by/4.0/>).

1. Introduction

In recent decades, intraplate volcanic eruptions were a priori interpreted as associated with deep mantle plumes, although alternative causes, such as abrupt lateral changes in stress at structural discontinuities of the lithosphere or the mantle global warming, were also advocated to explain the origin of some Large Igneous Provinces [1,2]. Less commonly hypothesized were tectonically generated melts as a result of decompression in the shallow lithospheric mantle or crust. Such interpretations were suggested for volcanic rocks from Cenozoic continental rifted areas of North America, Europe, Northeast Africa, and East Asia [3–17].

Volcanic rocks from the Baikal Rift System (BRS) have mainly OIB-like geochemical signatures, consistent with seismic tomography images that show low-velocity anomalies, possibly related to deep-seated magma sources occurring in the upper mantle and

transition layer. These could provide migrated volcanic eruptions through the moving lithosphere [18]. Meanwhile, volcanic rocks from the East Hangay Orogen and adjacent Orkhon-Selenga Saddle of Central Mongolia (southwestern part of the BRS) show both mantle and crustal components geochemically different from OIB [19]. Volcanic rocks of some eruption phases in the Kamar-Stanovoy zone of Hot Transtension (KSZHT) (central part of the BRS) and in the Vitim Plateau (northeastern part of the BRS) also indicate their generation in shallow (garnet-free) sources. Such volcanic rocks of basaltic andesite compositions in the latter area have, however, $^{143}\text{Nd}/^{144}\text{Nd}$ isotope ratio similar to that in high-Mg basanites, indicating the secondary high-degrees shallow melting of an OIB-like material previously raised from the lower-middle part of the upper mantle. At the eastern end of the Tunka Valley, few high-Mg basanite flows also erupted, but basaltic ones, derived from shallow sources, distinctly show no OIB-type signatures [20,21]. In this case, it is reasonable to assume melting of a material in a region of the crust-mantle transition (CMT). In order to recognize crustal and shallow mantle components, it is necessary, first of all, to define the local geochemical signatures of the crust.

Tectonic motions of the crust are accompanied with heat release resulted from friction during incremental sliding along a fault zone, in which an adhesive wear mechanism dominates. Generated melts of silicate rocks are quenched in planes of strong fault displacements as pseudotachylytes [22–26]. Tectonic pseudotachylytes were described in mylonites of various metamorphic environments that developed in a regime of dominant plastic deformation of the lower crust [27–30] and in cataclasites typical of brittle deformations in the middle and upper crust [31,32]. Minerals of igneous rocks and glass, preserved in pseudotachylytes of the upper crust, are affected by metamorphic transformations in deeper conditions [33–35].

On the one hand, the similarity of bulk chemical compositions of pseudotachylyte veins and host rocks led to an assumption on melt generation by complete melting of host rocks [22,36,37]. On the other hand, the presence of relict mineral fragments of quartz and feldspar (but not amphibole and mica) in most pseudotachylyte veins from different parts of the world showed predominant melting of mafic minerals [38–41]. High-friction experiments and numerical simulations of pseudotachylyte generation demonstrated the formation of a gouge of finely crushed material later filled with a melt generated by friction. Such a melt could interact with small debris with further melting of the material and a partial change in the original size of frictionally molten rock fragments. Some pseudotachylytes could have purely crushed origin [31,42–47]. In pseudotachylyte veins, a heterogeneous groundmass composition on a scale of microdomains was revealed, usually more mafic relative to a host rock bulk composition [39,48]. A composition of the pseudotachylyte matrix, enriched in mafic components, was explained by predominant crushing of softer mafic minerals during host rock cataclasis, followed by massive melting of a cataclasite [40,49].

A coefficient of volumetric expansion of a water is greater than in a host rock, therefore frictional heating causes an increase in pore pressure in a shear zone and, as a consequence, reduces the effective stresses, preventing melting that can only occur in a case of low permeability of a host rock and effective retention of a fluid under excessive pressure [50,51]. It remains unclear whether pseudotachylytes could be a result of melt penetration from a deeper root part of an active fault into its upper part.

In Southern Siberia, pseudotachylytes have been described so far only in the Primorye Fault that bounds the basement of the Siberian paleocontinent from terranes accreted in the southeast. It was inferred that this type of rocks inherited a chemical composition of a host diorite with relative depletion in SiO_2 and enrichments in FeO_{tot} , MgO , and CaO [52]. A new pseudotachylyte site is found in the Main Sayan Fault (MSF) that separates the southwestern margin of the Siberian paleocontinent basement from accreted terranes and spatially corresponds to the South Baikal Basin and Tunka Valley of the central Baikal Rift System (BRS) [53,54]. In 2003–2019, seismicity focused within the South Baikal Basin without propagating into the Tunka Valley. Earthquakes distributions and temporal

variations of $^{234}\text{U}/^{238}\text{U}$ activity ratio in groundwater indicated a future main seismic event of the 2020–2021 seismic reactivation in the South Baikal water area after an earthquake in the junction between the Tunka Valley and South Baikal Basin [55]. Respectively, the Bystraya earthquake ($K = 14.5$, $M_w = 5.4$) occurred on 21 September 2020 [56] and then the Selenga one followed on 9 December 2021 ($K = 13.9$).

The aim of this paper is to highlight significance of the deep-seated CMT magmatic sources for the structural development of the South Baikal Basin and Tunka Valley, presently affected by strong seismogenic deformations, through geochemical studies of the MSF pseudotachylytes and the KSZHT volcanic rocks. First, we consider the structural setting of magma generation and present results of the comparative analysis of pseudotachylyte and host mylonite compositions and then report results of the comparative study of the MSF pseudotachylytes and the KSZHT volcanic rocks to designate complementary relationships of their deep-seated sources.

2. Methods and Materials

In each volcano of the KSZHT, a sequence of lava layers was sampled from a base to a top. Data on compositions and ages of volcanic rocks, as well as compositions of their crystalline inclusions, were presented earlier [20,57–60]. For comparisons with the MSF pseudotachylytes, special attention was delivered to study compositions of lavas from the Kultuk and Meteo volcanoes. For understanding of volcanic activities in the entire hot transtension zone, rocks from the Karerny and Shirokiy volcanoes were additionally sampled. Pseudotachylytes were sampled in the MSF zone with their primary subdivision into rocks of basic, intermediate, and silicic geochemical/chemical compositions using a portable device to measure the magnetic susceptibility (produced by Geodevice Enterprise, Russia). In the KSZHT magma-controlling structure, syn-volcanic direction of extension was determined by the predominant orientation of dikes. Planes of main faults were reconstructed using the method of belts [61].

Major oxides of rock samples were determined by classical methods of analytical chemistry [62] and trace elements were analyzed by inductively-coupled plasma mass spectrometry (ICP–MS) using an Agilent 7500ce quadrupole mass spectrometer. Analytical results on major oxides and trace elements of the standard reference materials, obtained within the time interval of analyzing pseudotachylytes from the MSF and volcanic rocks from the KSZHT, are presented in Table S1 of the Supplementary Materials. Isotopic $^{87}\text{Sr}/^{86}\text{Sr}$ and $^{143}\text{Nd}/^{144}\text{Nd}$ ratios were measured on a Finnigan MAT 262 mass spectrometer. Standard reference materials JNd-1 (Japan) and NBS SRM-987 (USA) were used. Obtained during the period of measurements were $^{143}\text{Nd}/^{144}\text{Nd}$ value of 0.512104 ± 0.000004 (2σ) for JNd-1 and $^{87}\text{Sr}/^{86}\text{Sr}$ value of 0.710233 ± 0.000012 (2σ) for NBS SRM-987. Measurement results of samples were recalculated to the recommended values of the reference materials: 0.512103 and 0.71025, respectively [63]. A secondary alteration effect, causing distortion of $^{87}\text{Sr}/^{86}\text{Sr}$ values, was removed by treatment of samples by a 0.75 M hydrochloric acid solution for 24 h with its further removal through repeated washing by ultrapure water from an Elix-3 Millipore system (France). The methods applied were described previously by Rasskazov et al. [19] and Yasnygina et al. [64]. Analysis of Pb isotopes was performed by multiple-collector inductively coupled plasma mass spectrometry (MC-ICP-MS) using a Neptune Plus' mass spectrometer and the procedure of sample preparation described by Rasskazov et al. [11]. During the period of measurements, obtained values for NBS-981 were: $^{206}\text{Pb}/^{204}\text{Pb}$ 16.9378 ± 0.0011 , $^{207}\text{Pb}/^{204}\text{Pb}$ 15.4927 ± 0.0005 , and $^{208}\text{Pb}/^{204}\text{Pb}$ 36.6972 ± 0.0013 .

3. Structural Control of the South Baikal Basin and Tunka Valley, Structural Setting of Volcanism

The MSF pseudotachylyte site is located at a collisional border between the Khamardaban terrane and Siberian paleocontinent. The Slyudyanka paleocollision zone is designated by laterally changing degrees of metamorphism from granulite facies near the edge of the Siberian paleocontinent to greenschist ones in the inner part of the Khamardaban terrane.

This zonal metamorphism was resulted from the Early Paleozoic compression of the terrane crust against the rigid basement of the paleocontinent [65]. One more convergent phase was expressed by uplift and thrust of the Archean basement of the paleocontinent onto Jurassic sediments of the Irkutsk basin [66]. Later, the orogenic regime was retained in the South Baikal area in the Late Cretaceous and Paleogene [67].

The Slyudyanka paleocollision zone is inherited by the Tunka Valley. The western part of the South Baikal Basin, adjacent to the Tunka Valley, is bounded by the Obruchev fault in the north and by the SW Boundary Fault in the south. Along the faults, a crystalline bed of the basin was subsided for at least 5 km. Miocene-Quaternary bottom sediments, lying on a seismically isotropic basement, are as thick as 4 km. A rapid Pleistocene tectonic subsidence of the basin bed, which was not compensated by accumulation of sediments, was accompanied by 1 km deep water infilling [68–70].

The subsided South Baikal bed changes abruptly into the uplifted part of the Tunka Valley, where sedimentary and lava layers of the Miocene-Lower Pliocene Tankhoi Formation occupy high elevations of the relief at altitudes from 750 to 2000 m. The Upper Pliocene-Lower Pleistocene and Middle-Late Pleistocene sediments are also uplifted and partially eroded, although occupying lower relief elevations [57]. The vertical shift of sedimentary strata evidences on contrasting tectonic motions of the South Baikal Basin bed relative to the Tunka Valley. In the eastern end of the latter, volcanoes show an echelon-like combination of the Kamar and Stanovoy volcanic zones and the Bystraya one shifted for 20 km to the west (Figure 1). The KSZHT structure, defined by northeastern strike of dikes and chains of volcanoes in an area of about 600 km², designates extension of the crust directed along the MSF and constrained within the time interval of volcanic activities from 18.1 to 11.7 Ma [20].

Oblique extension (transtension) of the upper crust in the Kultuk village and its vicinity is evidenced from structural observations. Extension is indicated by normal faults (occasionally with lateral displacements) that are the main kinematic units in the BRS basins [71,72]. Transition from extension to compression is shown by thrusts and reverse faults (sometimes with lateral displacements) that displace coarse-clastic Pleistocene and Holocene sediments. Extension of the crust resulted in subsidence of the South Baikal Basin; its compression, on the contrary, led to uplift of the eastern part of the Tunka Valley.

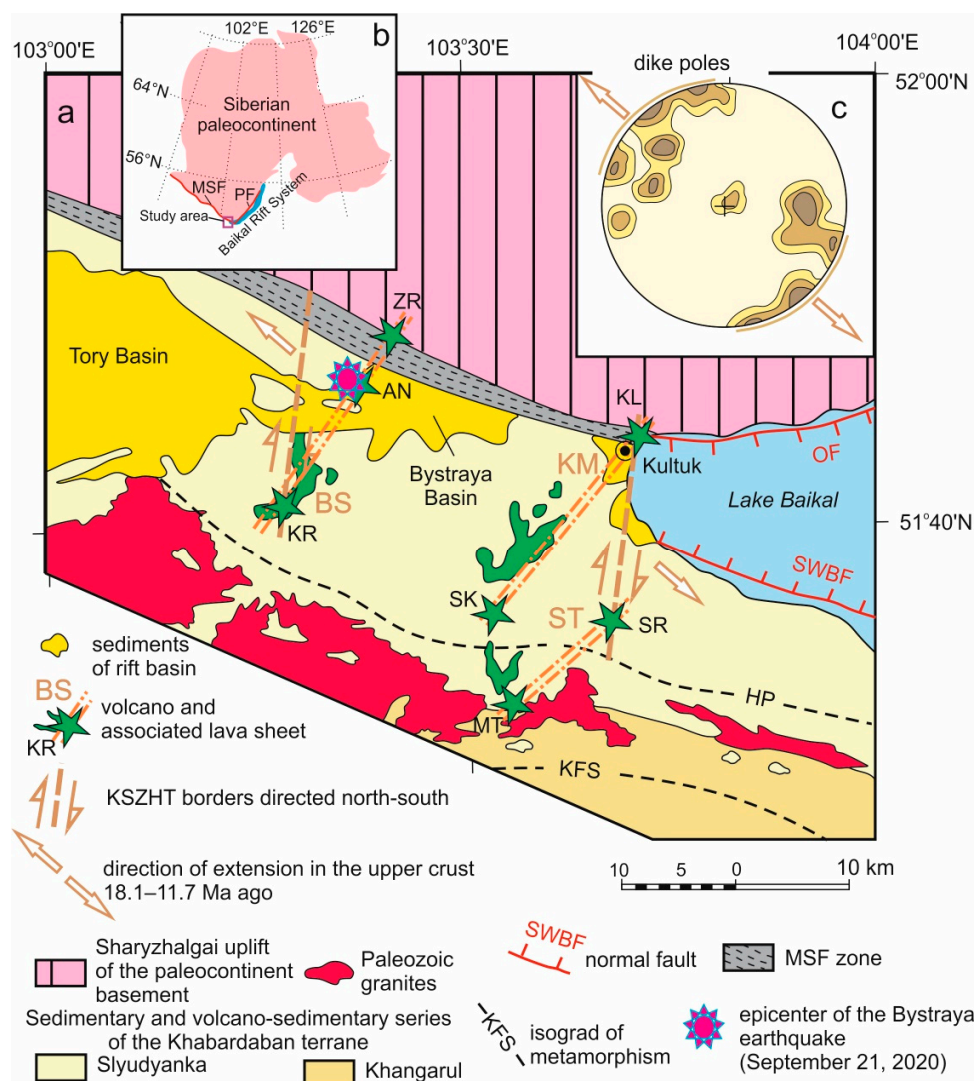


Figure 1. Geological map of the junction area between the lacustrine South Baikal Basin and Tunka Valley (a), location of the study area on the southern edge of the Siberian paleocontinent, bounded by the Main Sayan fault (MSF) and Primorye fault (PF) (b), and orientation of plane poles of the KSZHT dikes in the lower spherogram (c). Abbreviations: volcanoes and associated lava sheets: KR—Karerny, AN—Anchuk, ZR—Zyrkuzun, SK—Sukhoi, KL—Kultuk, MT—Meteo, and SR—Shirokiy; volcanic zones: Kamar (KM), Stanovoy (ST), and Bystraya (BS); normal faults: OF—Obruchev, SWBF—southwest boundary; isograds of metamorphism: KFS—potassic feldspar, HP—hypersthene. The geological scheme is modified after [65,73,74]. The spherogram is adopted from [54]. Density of points on the spherogram: 5%, 10%, and 15%.

4. Pseudotachylytes and Their Structural Setting

Pseudotachylytes are observed as a series of black and pink stripes and veins in solid-gray mylonites of an outcrop located 1 km west of the Kultuk village (Figure 2a). The stripes are as thick as 10 cm (Figure 2b). Pink bands are cut by black veins (Figure 2c). Unidirectional black banded series are accompanied by wedge-shaped (upwardly tapering) bodies of dark-gray pseudotachylytes. This kind of bodies is up to 2.5 m wide at the base (Figure 2d). Different parts of the outcrop show horizontal fractures filled by pistachio-green epidote-chlorite material. As a result of the most recent deformations, these fractures cut through all rocks.

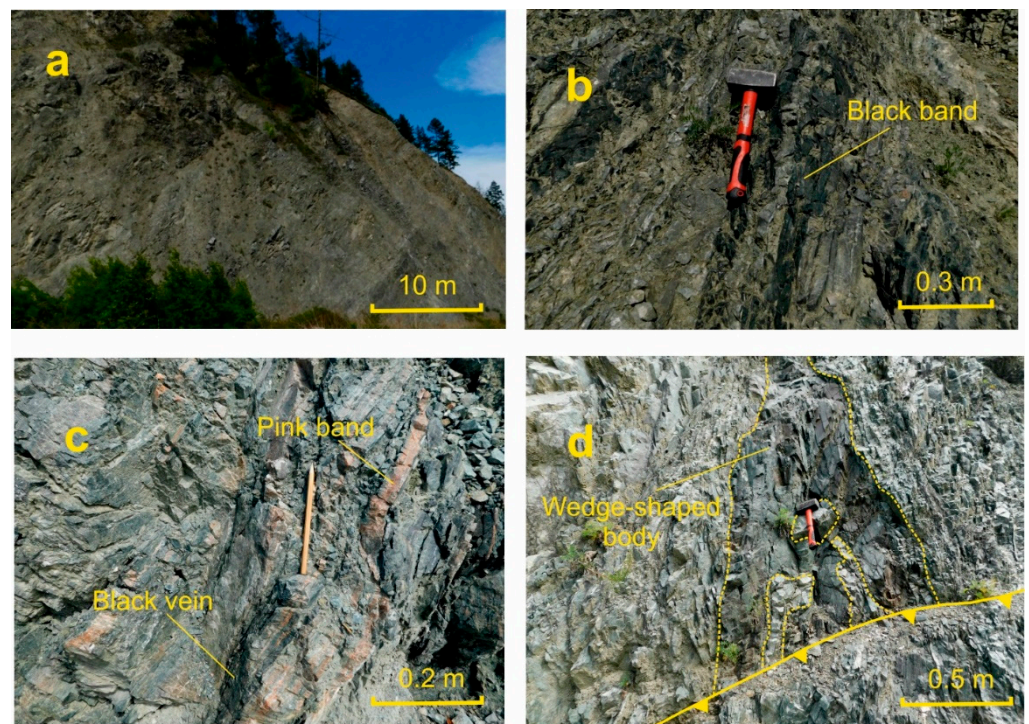


Figure 2. General view of the MSF outcrop located 1 km west of the Kultuk village (a), black band series (basic composition) (b), pink band series (silicic composition), cut by black veins (c), and a wedge-shaped body of dark-gray rock (intermediate composition) (d). In photograph a, dark saturated by injected rocks stripes dip under a slope of a quarry. In photograph d, a wedge-shaped fragment is cut at the base by a horizontal rupture.

Pseudotachylytes of different bodies are grouped in terms of magnetic susceptibility. Black bands of basic compositions show high magnetic susceptibility (3.4×10^{-3} – 6.17×10^{-2} SI units). Dark-gray wedge-shaped bodies and veins of intermediate compositions indicate lower magnetic parameters (3.36×10^{-4} – 5.71×10^{-4} SI units). Pink bands of silicic compositions yield interval of 3.17×10^{-5} – 4.80×10^{-5} SI units. Mylonites show a range of values from 9.04×10^{-5} – 2.70×10^{-4} SI units falling mainly between those of intermediate and silicic pseudotachylytes, although some massive mylonites show also elevated values.

Fracturing in a site of mylonites with black bands was studied to define inclinations of major fault planes using the method of belts [61]. Reconstructed are dips of two faults: 200° , angle of 74° and 274° , angle of 56° . The former has an azimuth of 290° that corresponds to the MSF strike; the latter designates the north-south direction of the KSZHT (Figure 3). The MSF plane dips from the Siberian platform to the south-southwest, under the Khamardaban terrane and the KSZHT plane from the South Baikal Basin to the west, under the Tunka Valley. A series of injected bands, veins, and wedge-shaped bodies extends almost parallel to the MSF plane with a relative clockwise turn by six degrees. Pseudotachylyte melts injected into antithetical fissures of the MSF hanging wing.

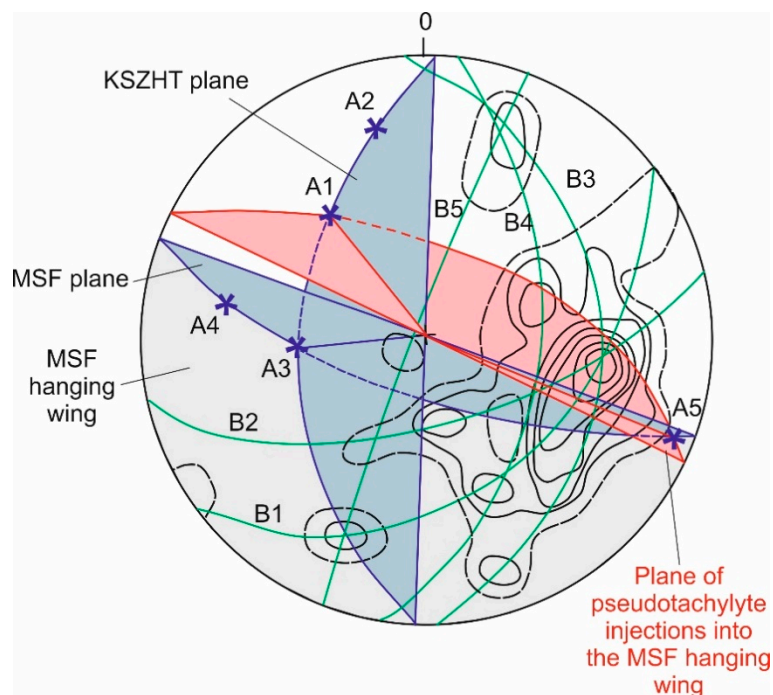


Figure 3. Outputs of axes of tectonic fractures in the MSF mylonites with reconstructed dips of the MSF and KSZHT planes in the lower hemisphere. Fracture belts B1, B2, B3, B4, and B5 correspond to the outlets of axes A1, A2, A3, A4, and A5, respectively. Orientations of 100 crack poles are plotted with a density of 13%, 11% . . . 3%, and 1%. Injected bands extend along the MSF plane. Injected bands, extended along the MSF plane, correspond to the antithetical fissures of its south-southwestern hanging wing.

5. Compositions of Pseudotachylytes and Host Mylonites

For analytical studies of the MSF rocks, samples of injected wedge-shaped bodies, veins, and bands, host mylonites (aluminosilicate and carbonate-aluminosilicate), and an epidote-chlorite rock were selected (Table 1). In a study the injected magmatic rocks, on the one hand, it is important to follow an experience of the pseudotachylyte classification as derivatives of seismogenic melts in faults. Therefore, the injected rock compositions are compared with those of two types of pseudotachylytes identified in the Sarwar-Junia Fault Zone, India: Pt I, from gneiss, and Pt II, from a contact between gneiss and metadolerite [32]. On the other hand, the injected rock compositions should be considered in terms of the nomenclature of non-crystallized volcanic rocks [75].

Table 1. Analytical results on representative samples of pseudotachylytes and mylonites from the MSF. MSF—Main Sayan Fault.

Sample	1	2	3	4	5	6	7	8	9
	KL-9	KL-23	KL-22	KL-1	KL-3	KL-11	KL-2	KL-5	KL-12
SiO ₂ , wt%	47.87	49.60	45.47	51.86	61.69	71.06	72.30	28.76	55.71
TiO ₂	1.76	1.62	0.60	0.69	0.89	0.11	0.08	0.55	0.59
Al ₂ O ₃	13.51	13.67	17.58	14.73	14.88	13.42	12.86	8.16	13.75
Fe ₂ O ₃	5.91	5.67	2.72	2.42	1.98	0.30	1.12	1.13	3.06
FeO	7.06	8.74	5.20	7.61	4.94	0.99	2.50	2.53	3.72
MnO	0.21	0.18	0.14	0.19	0.09	0.05	0.05	0.06	0.13
MgO	7.30	5.33	7.50	5.69	2.98	0.44	1.38	2.38	3.93
CaO	9.33	5.40	9.37	6.37	3.98	3.13	1.91	29.18	5.49
Na ₂ O	2.56	2.72	1.85	2.37	3.06	3.84	3.48	2.14	1.94
K ₂ O	0.65	0.50	1.12	0.87	2.67	4.32	1.62	1.10	3.20

Table 1. Cont.

Sample	1	2	3	4	5	6	7	8	9
	KL-9	KL-23	KL-22	KL-1	KL-3	KL-11	KL-2	KL-5	KL-12
P ₂ O ₅	0.36	0.15	0.12	0.08	0.21	0.04	0.02	0.20	0.18
H ₂ O [−]	0.08	0.07	0.07	0.20	0.14	0.06	0.14	0.20	0.38
H ₂ O ⁺	3.21	4.21	4.76	4.36	1.85	1.35	1.70	1.93	5.76
CO ₂	0.37	2.20	3.39	2.40	0.41	1.11	0.61	21.80	1.83
Total	100.18	100.06	99.89	99.84	99.77	100.22	99.77	100.12	99.67
Sc, ppm	45.9	41.2	31.2	43.8	19.6	4.2	15.7	7.4	27.8
V	395	404	184	354	122	15	73	69	203
Cr	239	46	250	196	108	12.2	44	21	107.9
Co	47	42	29	28	20.1	2.9	6.7	9.3	21.6
Ni	116	32	115	52	50	6.3	16	24	39
Cu	52	30	60	59	76	10	33	<10	28
Zn	105	71	69	70	68	16	56	96	60
Ga	17.7	18.1	13.7	14.9	20.3	16.0	10.8	9.2	19.3
Rb	14	14.4	28.2	29	79	92	59	31	159
Sr	529	273	362	279	701	408	154	1812	146
Y	32.8	41.0	12.0	22.8	34.3	12.3	11.4	15.2	17.5
Zr	28	5.0	11.0	44	35	32	13	23	9.4
Nb	4.3	1.6	1.5	1.78	13.9	8.4	3.11	8.69	2.2
Cs	0.5	0.46	0.50	0.6	1.4	0.5	1.5	5.7	6.3
Ba	371	170	315	236	1457	961	624	525	426
La	18.7	2.44	4.66	3.45	74.5	15.3	3.13	22.7	5.9
Ce	44.0	8.25	11.0	8.60	156.2	29.7	7.91	44.9	14.4
Pr	6.00	1.63	1.59	1.41	17.19	3.34	1.19	5.54	1.99
Nd	26.0	9.23	7.27	6.68	64.1	12.4	5.37	21.7	9.43
Sm	6.10	3.55	2.05	2.25	11.07	2.37	1.55	4.19	2.62
Eu	1.91	1.31	0.71	0.80	2.58	0.52	0.30	1.10	0.93
Gd	6.22	4.99	2.06	3.20	8.55	2.04	1.74	3.68	3.09
Tb	1.01	0.96	0.35	0.56	1.11	0.31	0.31	0.50	0.52
Dy	6.01	6.72	2.22	3.75	6.54	2.02	1.94	2.84	3.25
Ho	1.26	1.45	0.46	0.80	1.27	0.43	0.41	0.53	0.61
Er	3.54	4.41	1.32	2.50	3.50	1.26	1.24	1.48	1.85
Tm	0.47	0.68	0.21	0.38	0.52	0.20	0.18	0.21	0.27
Yb	3.01	4.34	1.12	2.43	3.18	1.22	1.31	1.26	1.58
Lu	0.45	0.67	0.18	0.37	0.48	0.19	0.21	0.19	0.21
Hf	0.96	0.56	0.53	0.58	1.22	1.38	0.48	0.70	0.44
Ta	0.28	0.29	0.14	0.13	0.83	0.67	0.25	0.51	0.15
Pb	3.6	N.d.	3.4	N.d.	29.3	23.3	5.3	10.8	3.6
Th	2.67	0.11	0.63	0.55	14.7	2.81	0.49	4.19	0.92
U	0.57	0.04	0.15	0.16	1.55	0.55	0.17	2.88	0.56

Pseudotachylyte compositions: 1–2, basic, moderate-Ti basalt; 3–4, basic, low-Ti basalt; 5, intermediate, dacite; 6, silicic, rhyolite. Mylonite compositions: 7, aluminosilicate; 8, carbonate-aluminosilicate. 9, epidote-chlorite rock. N.d., not determined. All analytical results on pseudotachylytes and mylonites from the MSF are presented in Table S2 of Supplementary Materials.

Samples of black stripes that correspond to basic compositions in terms of a SiO₂ content are subdivided into moderate- and low-Ti groups (TiO₂ contents 1.43–2.18 wt% and 0.6–0.69 wt%, respectively). Sample KL-17 with the lowest MgO content (4.17 wt%) of the moderate-Ti group has a reduced (but not the lowest) TiO₂ content (1.77 wt%). Specifically referred is sample KL-21, which shows TiO₂ = 1.28 wt% and MgO = 5.18 wt% between contents of these oxides in the moderate- and low-Ti groups. In terms of SiO₂, Al₂O₃, MgO, and TiO₂ abundances, these rocks are comparable to the type II pseudotachylyte from the Sarwar-Junia Fault Zone, but differ from it by elevated Na₂O and reduced FeO_{tot} and K₂O contents (Figure 4). In a thin section of the basic pseudotachylyte, shown in Figure 2b, a foliated groundmass composed of glaucophane, quartz, and magnetite is observed (Figure 5a). Obviously, this rock, originally solidified from an injected basaltic melt, was affected by metamorphism.

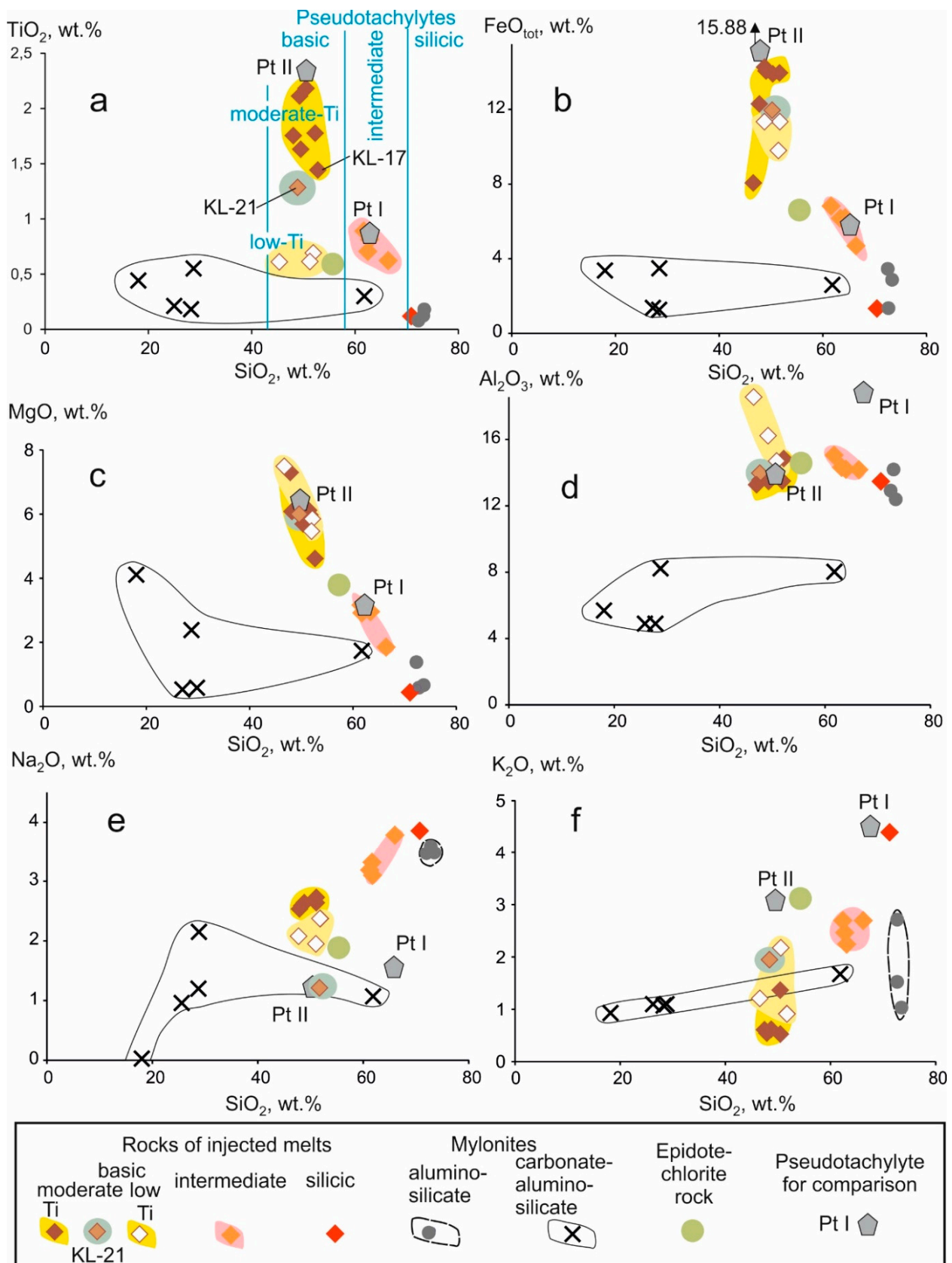


Figure 4. Grouping of rocks of injected melts and mylonites and their relationships with the epidote-chlorite rock from the MSF on diagrams of SiO₂ plotted versus oxides: (a) TiO₂, (b) FeO_{tot}, (c) MgO, (d) Al₂O₃, (e) Na₂O, and (f) K₂O. Shown for comparisons are two types of pseudotachylyte compositions: Pt I from gneiss; Pt II from a contact between gneiss and metadolerite [32]. In diagrams, measured major oxide values are used.

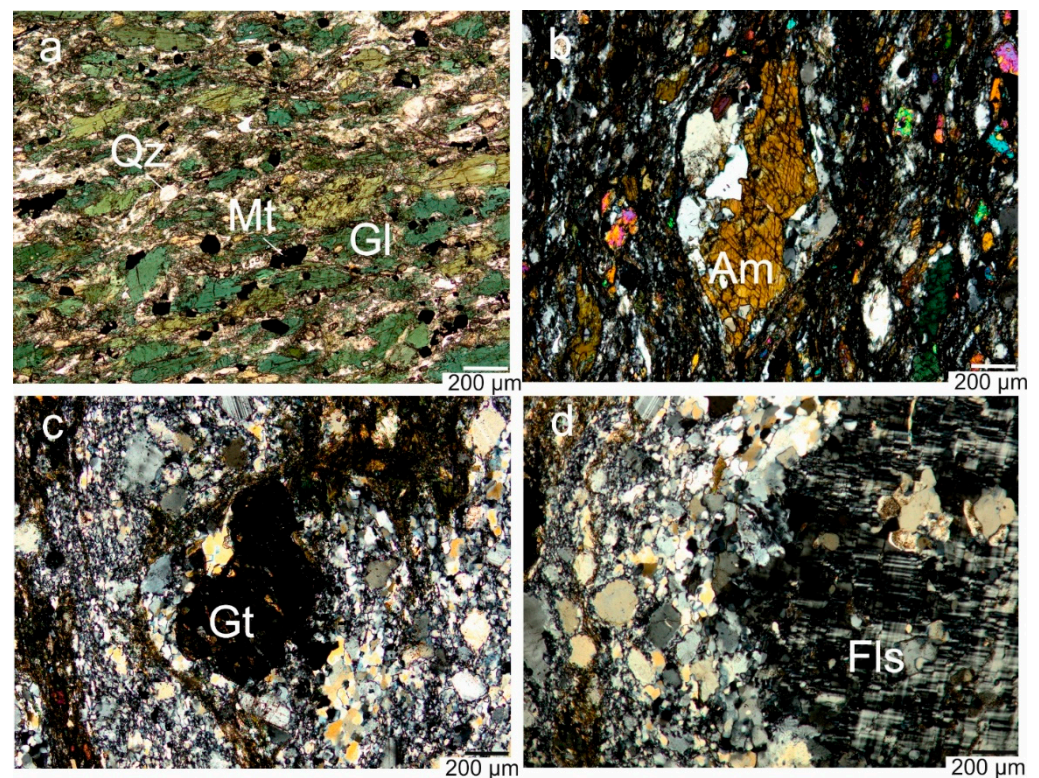


Figure 5. Microscopic observations of thin sections: (a) glaucophane-quartz-magnetite schist (Gl-Qz-Mt) after pseudotachylyte of basic composition (type II) in sample KL-9 (plane polarized light); (b–d) large grains of minerals in a quartz-feldspar aggregate that replaces pseudotachylyte of dacite composition (type I): amphibole (Am) in sample KL-17 from a vein (b), garnet (Gt), and potassic feldspar (Fls) (c and d, respectively) in sample KL-3 from a wedge (crossed polarized light). 200 µm scale bar shown in each microphotograph.

Samples, taken from individual wedge-shaped bodies, show an SiO_2 range of 61.69–66.43 wt% with total alkalis of 5.73–6.47 wt%. These rocks have intermediate (andesite and dacite) compositions. When recalculated to 100% without loss on ignition, all rocks are dacites. The MgO and FeO_{tot} contents in these rocks (1.85–3.18 wt% and 4.77–6.72 wt%, respectively) are lower than in basic pseudotachylytes. In terms of SiO_2 , MgO , CaO , and FeO_{tot} contents, these rocks are comparable to the type I pseudotachylyte from the Sarwar-Junia Fault Zone, but differ from it by elevated Na_2O and reduced Al_2O_3 and K_2O contents (Figure 4). Thin sections of these rocks show large grains of amphibole, garnet, and microcline, surrounded by a fine-grained strongly deformed quartz-feldspar groundmass (Figure 5b–d).

Pink bands and veins have silicic (rhyolite) compositions with low MgO , FeO_{tot} , CaO and elevated Na_2O and K_2O contents. The banding style of these rocks indicates structural conditions of their generations similar to those of basic pseudotachylytes. The pink injected rocks are compositionally distinguished from those of the types I and II in the Sarwar-Junia Fault Zone and are referred to the type III.

Mylonites are composed of a mixed aluminosilicate and carbonate rubbed material. Carbonate is present both in bulk mylonites and in veins. The aluminosilicate mylonite group contains 72.3–73.4 wt% SiO_2 . As SiO_2 of this group increases, MgO , FeO_{tot} , CaO , Al_2O_3 , and K_2O decrease, while Na_2O increases. The carbonate-aluminosilicate mylonite group shows 18.0–61.8 wt% SiO_2 . In this group, increase of SiO_2 content is also accompanied by decrease of MgO , FeO_{tot} , and CaO abundances, but the K_2O content consistently increases. A sample with the lowest SiO_2 content (KL-7) has a negligible Na_2O concentration (0.2 wt%) with Al_2O_3 content as low as 5.7 wt%. In other samples of the carbonate-aluminosilicate group, Na_2O abundance is also relatively low (1.08 wt% and

2.14 wt%). An epidote-chlorite rock shows TiO_2 , FeO_{tot} , and MgO contents that lower than values of basic pseudotachylytes but higher than those of mylonites. This could result from mechanical mixing between different materials in the fault zone. However, other oxides do not fit this simple mixing. For instance, K_2O abundance of the epidote-chlorite rock, which is as high as 3.2 wt%, exceeds its values in both basic pseudotachylytes and mylonites (Figure 4).

The subdivision of the MSF samples into mylonites and pseudotachylytes in terms of major oxide abundances is consistent with their grouping in terms of trace-element signatures. On a $MgO - Th/U$ diagram (Figure 6), illustrated are a high Th/U ratio (5–10) in intermediate pseudotachylytes, its value about 5 in a silicic pseudotachylyte (sample KL-11), and interval of 2.5–6.0 in basic pseudotachylytes. The Th/U ratio of mylonites and epidote-chlorite rock varies from 1.5 to 3.5.

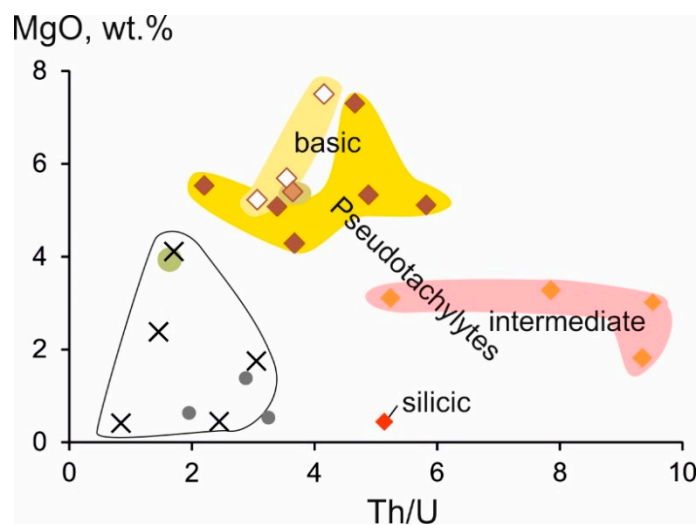


Figure 6. Pseudotachylytes, mylonites, and epidote-chlorite rock from the MSF on a $MgO-Th/U$ diagram. Symbols are as in Figure 4.

The moderate- and low-Ti groups of basic pseudotachylytes indicate distinctly different distribution of rare earth elements (REE) (Figure 7a). Moderate-Ti samples KL-19,20 show chondrite-like patterns. Other moderate-Ti samples KL-9,17 and KL-23,24 demonstrate chondrite-normalized spectra enriched and depleted in light REE, respectively. Low-Ti pseudotachylytes have lower REE abundances. Their chondrite-normalized spectra show weak depletion and enrichment in heavy REE. The transitional sample KL-21 falls between the moderate- and low-Ti groups. All basic pseudotachylytes show no Eu anomaly. Pseudotachylytes of intermediate and silicic compositions have light-REE-rich patterns with distinct Eu troughs (Figure 7b).

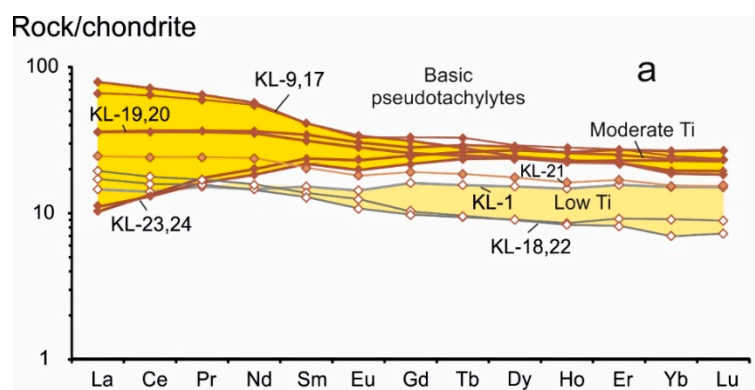


Figure 7. Cont.

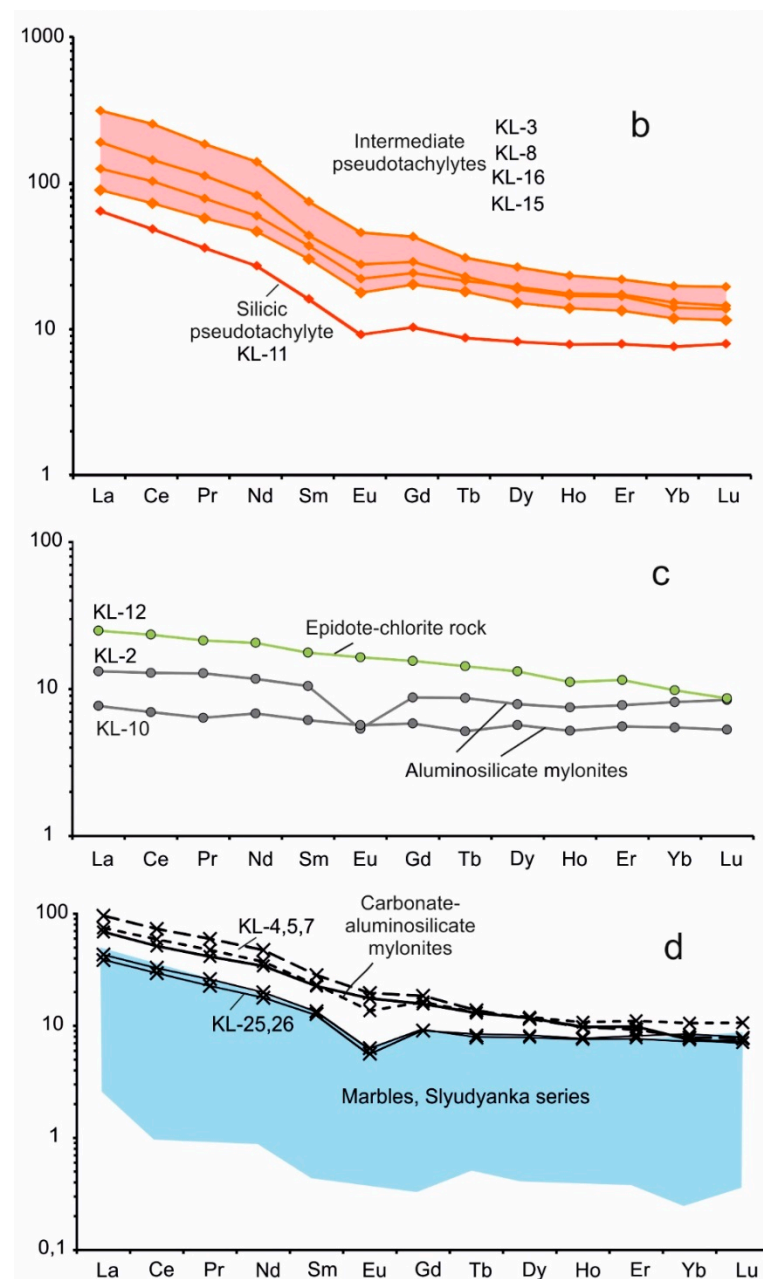


Figure 7. Chondrite-normalized REE spectra of rocks from the MSF: (a) basic pseudotachylytes; (b) intermediate and silicic pseudotachylytes; (c) aluminosilicate mylonites and epidote-chlorite rock; (d) carbonate-aluminosilicate mylonites. Shown for comparison in panel c is the range of carbonate rocks of the Slyudyanka complex (without fine-crystalline marbles with lower REE abundances) [76]. For normalization, the chondrite composition was used after [77].

Aluminosilicate mylonites have unenriched or slightly enriched REE spectra with and without Eu anomaly. A line of the epidote-chlorite rock extends above those of aluminosilicate mylonites (Figure 7b). Carbonate-aluminosilicate mylonites show a weak enrichment in light REE. The analyzed samples yield a range of normalized concentrations at the upper limit of the marbles from the Slyudyanka crystalline complex and slightly shift above them (Figure 7d).

Correlation between $\text{CaO}/\text{Al}_2\text{O}_3$ and CO_2 (Figure 8a) emphasizes a sufficient role of a carbonate mineral phase in the carbonate-aluminosilicate group and its decreasing in the aluminosilicate one. Common trends of mylonites on $\text{CaO}/\text{Al}_2\text{O}_3\text{-CO}_2$, $\text{CaO}/\text{CO}_2\text{-CO}_2$, and $\text{Ba}/\text{Sr-CO}_2$ diagrams (Figure 8a,b,d) indicate a mechanical mixing of an aluminosilicate

material (with low CaO content and high Ba/Sr ratio) and a carbonate one (with high CaO content and low Ba/Sr ratio). A deviation from the mixing trend of a single data point of mylonite KL-10 indicates an admixture of magmatic material processed into mylonites. All pseudotachylytes definitely deviate from the mylonite trend of carbonate admixture and incorporate variable proportions of carbonate phase.

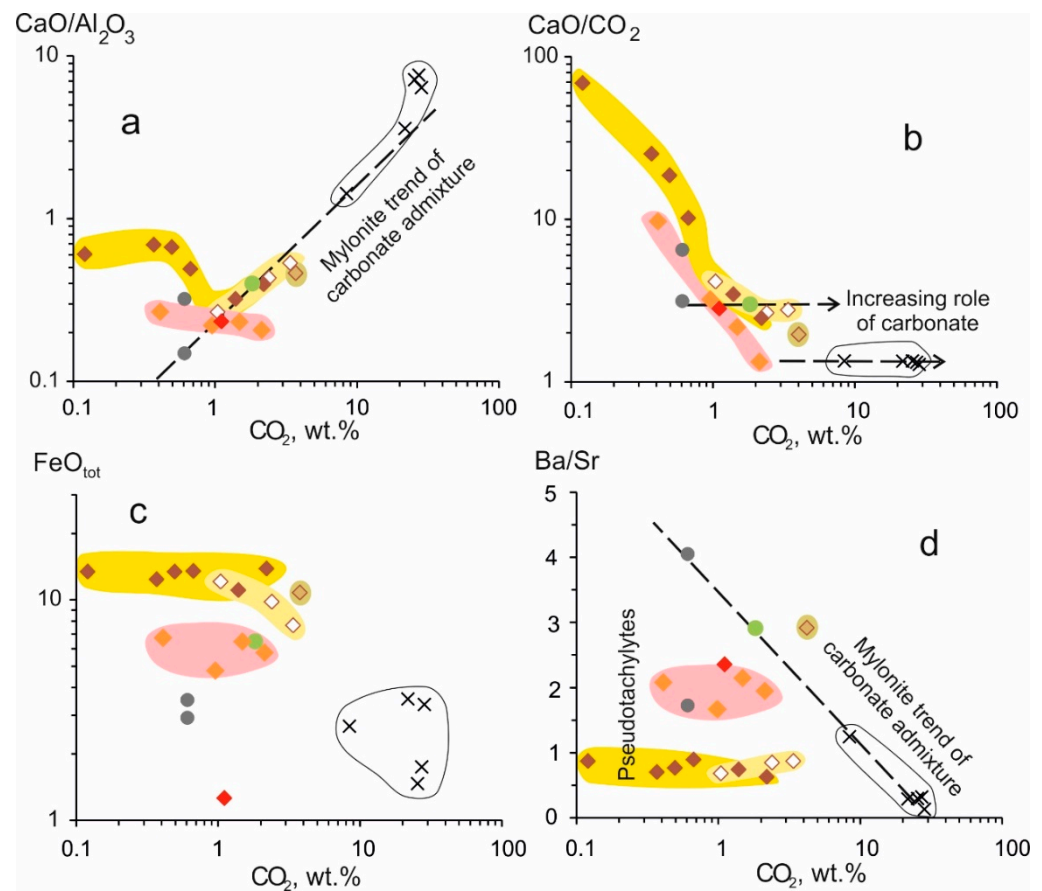


Figure 8. Pseudotachylytes, mylonites, and epidote-chlorite rock from the MSF on diagrams of CO_2 plotted versus: (a) $\text{CaO}/\text{Al}_2\text{O}_3$, (b) CaO/CO_2 , (c) FeO_{tot} , and (d) Ba/Sr . In diagrams, measured major oxide values are used. Symbols are as in Figure 4.

6. Compositions of Basic Pseudotachylytes and Volcanic Rocks

The defined three types of pseudotachylytes in one outcrop and the difference of their compositions from those of host mylonites may indicate their generation in different sources of the MSF root and ascending of melts to an upper common level. These kinds of deep-seated sources for basic pseudotachylytes might have links with those for the KSZHT volcanic rocks.

6.1. Major Oxides

Volcanic rocks from the KSZHT vary from silica saturated basalts to strongly undersaturated basanites. Basaltic lavas erupted on the Kultuk and Meteo volcanoes. The former occurred directly in the MSF zone and was active both at the beginning and at the end of the KSZHT volcanism (about 18 and 13 Ma), the latter was the farthest one from the MSF to the south and was active only at the beginning of the KSZHT volcanism (18.1–17.6 Ma).

Compared with volcanic rocks (Table 2), basic pseudotachylytes have a lower MgO content. Since abundance of this oxide in a melt is functionally dependent on temperature [78–80], the MSF pseudotachylyte melts had obviously lower temperatures than those of the KSZHT. On a $\text{MgO}-\text{SiO}_2$ diagram (Figure 9a), data points of pseudotachylyte

samples KL-22 and KL-9 with the highest MgO content are plotted close to volcanic rocks with the lowest content of this oxide. Consequently, temperatures of melts quenched into pseudotachylytes KL-22 and KL-9 were comparable with minimal temperatures of erupted basaltic melts. Low-Ti pseudotachylyte KL-22 shows a lower SiO₂ content than moderate-Ti pseudotachylyte KL-9. Other low- and moderate-Ti pseudotachylytes show intersecting trends of increasing SiO₂ and decreasing MgO abundances

Table 2. Analytical results on representative samples of volcanic rocks from the KSZHT (Kamar-Stanovoy Zone of Hot Transtension).

Volcano	Meteo			Kultuk		Karerny	Shirokiy
Age, Ma	18.1	17.7	17.6	18	13	13	13
Sample	687/2	684/1	683/4	Klt-12	Klt-9	15-04	SL16-1
SiO ₂ , wt%	49.62	47.99	47.78	48.26	48.26	44.77	44.38
TiO ₂	2.28	2.40	2.67	2.24	1.95	2.73	2.72
Al ₂ O ₃	14.10	14.90	14.9	14.71	15.15	13.39	13.38
Fe ₂ O ₃	2.52	2.37	3.2	2.96	3.59	2.23	2.92
FeO	8.85	9.24	8.72	7.46	7.95	9.42	9.29
MnO	0.16	0.15	0.15	0.13	0.14	0.17	0.18
MgO	7.85	7.88	8.1	8.20	8.06	10.44	9.72
CaO	8.13	7.98	7.98	7.62	8.00	9.86	9.53
Na ₂ O	2.94	3.22	3.6	2.94	3.26	2.98	2.95
K ₂ O	1.40	1.48	1.85	1.69	1.09	1.72	1.63
P ₂ O ₅	0.43	0.50	0.56	0.58	0.34	0.66	0.59
H ₂ O ⁻	0.22	0.82	0.6	0.72	0.51	0.21	0.16
H ₂ O ⁺	1.87	1.40	0.9	2.49	1.67	1.80	2.71
Total	100.37	100.33	101.01	100.00	99.97	100.38	100.16
Sc, ppm	21.4	22.0	18.7	24.3	29.2	14.5	19.4
V	N.d.	N.d.	N.d.	173	197	218	251
Cr	N.d.	N.d.	N.d.	281	201	251	222
Co	N.d.	N.d.	N.d.	44	48	51	56
Ni	N.d.	N.d.	N.d.	127	125	196	172
Cu	51	39	55	41	58	45	59
Zn	126	147	126	119	111	126	133
Ga	N.d.	N.d.	N.d.	21.5	20.5	20.0	21.2
Rb	17	19	24	15	11	35	29
Sr	2015	620	745	1301	447	1129	764
Y	22.2	24.1	23.6	20.5	21.0	22.5	21.0
Zr	198	231	246	188	166	202	224
Nb	27.45	38.54	40.71	32.37	21.26	55.24	45.42
Cs	N.d.	N.d.	0.42	0.28	0.13	0.36	0.20
Ba	402	322	427	281	213	432	388
La	19.8	24.1	31.3	23.7	16.0	35.1	32.0
Ce	45.0	50.3	65.7	51.3	34.9	76.1	69.0
Pr	5.28	6.05	8.20	6.65	4.65	8.92	8.34
Nd	25.95	29.16	34.18	28.36	20.42	36.18	33.92
Sm	5.66	6.48	7.72	6.57	4.99	7.82	7.09
Eu	1.86	2.04	2.29	2.14	1.72	2.47	2.36
Gd	5.46	6.11	6.67	5.77	4.98	7.14	6.49
Tb	0.79	0.87	0.95	0.86	0.75	1.00	0.96
Dy	4.28	4.43	5.20	4.33	4.22	5.24	4.58
Ho	0.75	0.80	0.94	0.81	0.82	0.85	0.80
Er	2.07	2.06	2.23	2.03	2.10	2.17	1.91
Tm	N.d.	N.d.	0.33	0.27	0.29	0.28	0.25
Yb	1.59	1.66	1.78	1.50	1.73	1.49	1.46
Lu	0.25	0.25	0.26	0.20	0.23	0.21	0.20
Hf	4.33	4.93	5.90	4.73	4.36	5.06	5.12
Ta	1.59	2.34	2.81	1.93	1.36	3.89	2.92
Pb	2.5	2.7	4.6	5.4	3.6	2.1	1.9
Th	1.97	2.39	3.41	2.06	1.81	4.54	3.27
U	0.26	0.73	0.95	0.74	0.50	1.63	0.82
⁸⁷ Sr/ ⁸⁶ Sr	0.704676	0.704362	0.704279	0.704493	0.704523	N.d.	N.d.
±2σ	0.000009	0.000010	0.000013	0.000013	0.000016		
¹⁴³ Nd/ ¹⁴⁴ Nd	0.512683	0.512705	0.512711	N.d.	N.d.	N.d.	N.d.
±2σ	0.000009	0.000017	0.000010				

Table 2. Cont.

Volcano	Meteo			Kultuk		Karerny	Shirokiy
Age, Ma	18.1	17.7	17.6	18	13	13	13
Sample	687/2	684/1	683/4	Klt-12	Klt-9	15-04	SL16-1
$^{206}\text{Pb}/^{204}\text{Pb}$	17.6474	17.8789	17.8163	17.7734	17.7096	18.1204	18.1591
$\pm 2\sigma$	0.0020	0.0013	0.0022	0.0034	0.0020	0.0025	0.0030
$^{207}\text{Pb}/^{204}\text{Pb}$	15.4674	15.5014	15.4849	15.4736	15.4787	15.5111	15.5212
$\pm 2\sigma$	0.0019	0.0012	0.0020	0.0030	0.0019	0.0022	0.0025
$^{208}\text{Pb}/^{204}\text{Pb}$	37.8221	38.0072	37.9359	37.8037	37.9245	38.1196	38.1885
$\pm 2\sigma$	0.0046	0.0030	0.0048	0.0075	0.0042	0.0055	0.0065

N.d., not determined. All analytical results on volcanic rocks from the Kultuk, Meteo, Karerny, and Shirokiy volcanoes are presented in Tables S3 and S4 of Supplementary Materials.

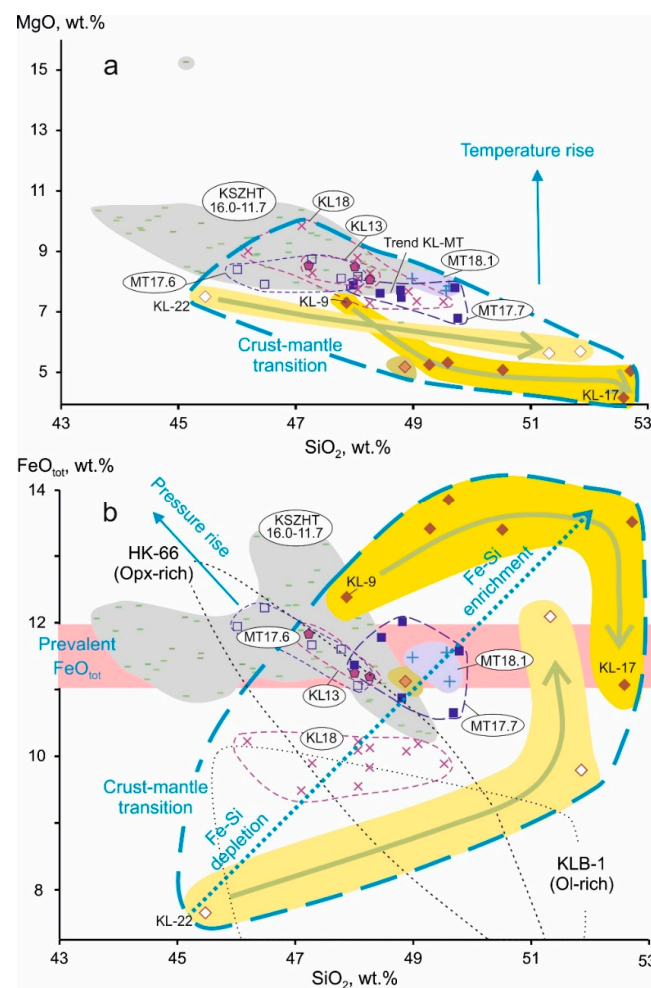


Figure 9. Comparisons of basic pseudotachylytes from the MSF and volcanic rocks from the KSZHT on MgO-SiO_2 (a) and $\text{FeO}_{\text{tot}}\text{-SiO}_2$ (b) diagrams. In diagrams, measured major oxide values are plotted. Among the KSZHT rocks, specifically distinguished are those of initial and final eruptions of the Kultuk Volcano in the MSF about 18 and 13 Ma (designated as KL18 and KL13, respectively), three phases of the Meteo Volcano (18.1, 17.7, and 17.6 Ma, designated as MT18.1, MT17.7, and MT17.6, respectively) that is the farthest from the MSF, and time-intermediate eruptions of the Karerny, Sukhoi, and Shirokiy volcanoes (designated as KSZHT 16.0–11.7) that arrange along a west-east line occurred between the Kultuk and Meteo volcanoes (Figure 1). Symbols of the MSF low- and moderate-Ti basic pseudotachylytes are as in Figure 4. Shown for comparisons are also data fields of melts experimentally generated from the lherzolites enriched in olivine (KLB-1) and orthopyroxene (HK-66) with pressure rise [81].

On a $\text{FeO}_{\text{tot}}\text{-SiO}_2$ diagram (Figure 9b), volcanic rocks and basic pseudotachylytes yield a prevalent FeO_{tot} interval of 11–12 wt% under SiO_2 content ranging from 44 to 53 wt%. Compositions of the Meteo Volcano are in a range of the prevalent FeO_{tot} interval. Initial (18.1 Ma) lavas yield data points compactly enclosed within a data field of those represented the second (17.7 Ma) eruption phase, while points of the third (17.6 Ma) eruption phase demonstrate a shift along the prevalent FeO_{tot} interval to the KSZHT compositions with a lower SiO_2 content. Data points of the initial (18 Ma) lavas from the Kultuk Volcano show FeO_{tot} abundance below the prevalent FeO_{tot} interval, while points of the final (13 Ma) lavas from this volcano overlap those of the 17.6 Ma phase of the Meteo Volcano.

Compared with the KSZHT volcanic rocks, basic pseudotachylytes show broader SiO_2 and FeO_{tot} variations. The low- and moderate-Ti groups indicate opposite trends of enrichment and depletion in SiO_2 and FeO_{tot} relative to the prevalent FeO_{tot} interval. Moderate-Ti sample KL-9 with elevated MgO content shows increase in FeO_{tot} and decrease in SiO_2 contents relative to the MT18.1 data field. Similar trend was obtained experimentally with increasing pressure for melts from orthopyroxene-enriched lherzolite HK-66 [81]. Data point of low-Ti sample KL-9 with elevated MgO content shifts relative to the MT18.1 data field with a relative decrease in both FeO_{tot} and SiO_2 contents. The KL18 data field falls on this trend. Moderate-Ti pseudotachylytes also show increasing FeO_{tot} content as SiO_2 content increases from sample KL-9. At the lowest MgO content, sample KL-17 shows the FeO_{tot} value in a range of the prevalent compositions.

6.2. La/Yb Ratio

In the Tunka Valley, basaltic and basanitic melts brought to the surface polycrystalline garnet-free cognate inclusions and xenoliths extracted from walls of magma conduits. The crystalline nodules from volcanic rocks incorporated olivine, ortho- and clinopyroxene, spinel, plagioclase, amphibole, and mica [57,60]. A garnet-bearing material, not represented by crystalline inclusions and shown only by erupted melts, are referred to as a deeper region [20,57]. Generally, basic pseudotachylytes and volcanic rocks from the Meteo and Kultuk volcanoes could be generated in the deep-seated CMT sources, while volcanic rocks from the Karerny and Shirokiy volcanoes with lower SiO_2 content than in rocks of the Meteo and Kultuk volcanoes could be produced in sources of the deeper lithospheric mantle.

Respectively, the transition from a garnet-bearing material to a garnet-free one can be considered as the crust–mantle boundary. A similar transition was suggested for Southeastern Australia, where the Moho boundary, determined from seismic data at a depth about 55 km, was compared with the same depth, estimated from a spinel–garnet transition in lherzolite xenoliths [82].

Garnet-free and garnet-bearing deep-seated sources of the KSZHT volcanic rocks were calculated through trace-element modeling of equilibrium melting [20]. It was shown that hypersthene-normative basaltic lavas, erupted on the Meteo Volcano 18.1–17.7 Ma, were generated in a garnet-free source with high degrees of melting ($F = 0.15\text{--}0.23$). Nepheline-normative basalts of this volcano, erupted 17.6 Ma, were modeled as derivatives of a garnet-bearing source with moderate degrees of melting ($F \sim 0.08$). For 18 Ma and 13 Ma basalts from the Kultuk Volcano, garnet-bearing and garnet-free deep-seated sources were defined, respectively. Therefore, the beginning of hot transtension was perceived by activities of separate garnet-free and garnet-bearing sources of the Meteo and Kultuk volcanoes, while the end of hot transtension was spotted by activities of a garnet-free one in the Kultuk Volcano.

From results of modeling, melts of garnet-bearing and garnet-free deep-seated sources were discriminated by a $(\text{La}/\text{Yb})_{\text{N}}$ ratio of 9.5 (normalization to the pyrolite [77]). The values >9.5 and <9.5 were defined as indicators of garnet-bearing (mantle) and garnet-free (crustal) sources, respectively. The $(\text{La}/\text{Yb})_{\text{N}}$ ratio is used further for a gradation of the KSZHT melts from relatively low degrees of melting in a deeper lithospheric mantle source ($F \sim 0.05$, $(\text{La}/\text{Yb})_{\text{N}} = 13\text{--}18$), through elevated degrees of melting in a sub-crustal

level ($F \sim 0.08$, $(La/Yb)_N = 10-12$) to higher degrees of melting at the base of the crust ($F = 0.15-0.23$, $(La/Yb)_N = 10-12$) (Figure 10a).

Melting of the MSF basic pseudotachylytes also fits into the same gradation (without modeling, $(La/Yb)_N < 4$). Comparison of basic pseudotachylytes from the MSF with the one from the contact between gneiss and metadolerite in the Sarvar-Juniya fault zone [32] indicates their comparable SiO_2 , Al_2O_3 , MgO , and CaO , but different FeO_{tot} , K_2O , and Na_2O contents (Figure 4). The similarity of the former four components may indicate their distribution that obeys intensive (PT) parameters of tectonic generations of silicate melts, while the discrepancy between the latter three components may indicate their additive distribution, i.e., displaying of extensive (concentration) parameters of tectonic generation of silicate melts. Consequently, the FeO_{tot} , K_2O , and Na_2O contents in tectonically generated melts could reflect complementary redistribution of these components in the lithospheric mantle and crust.

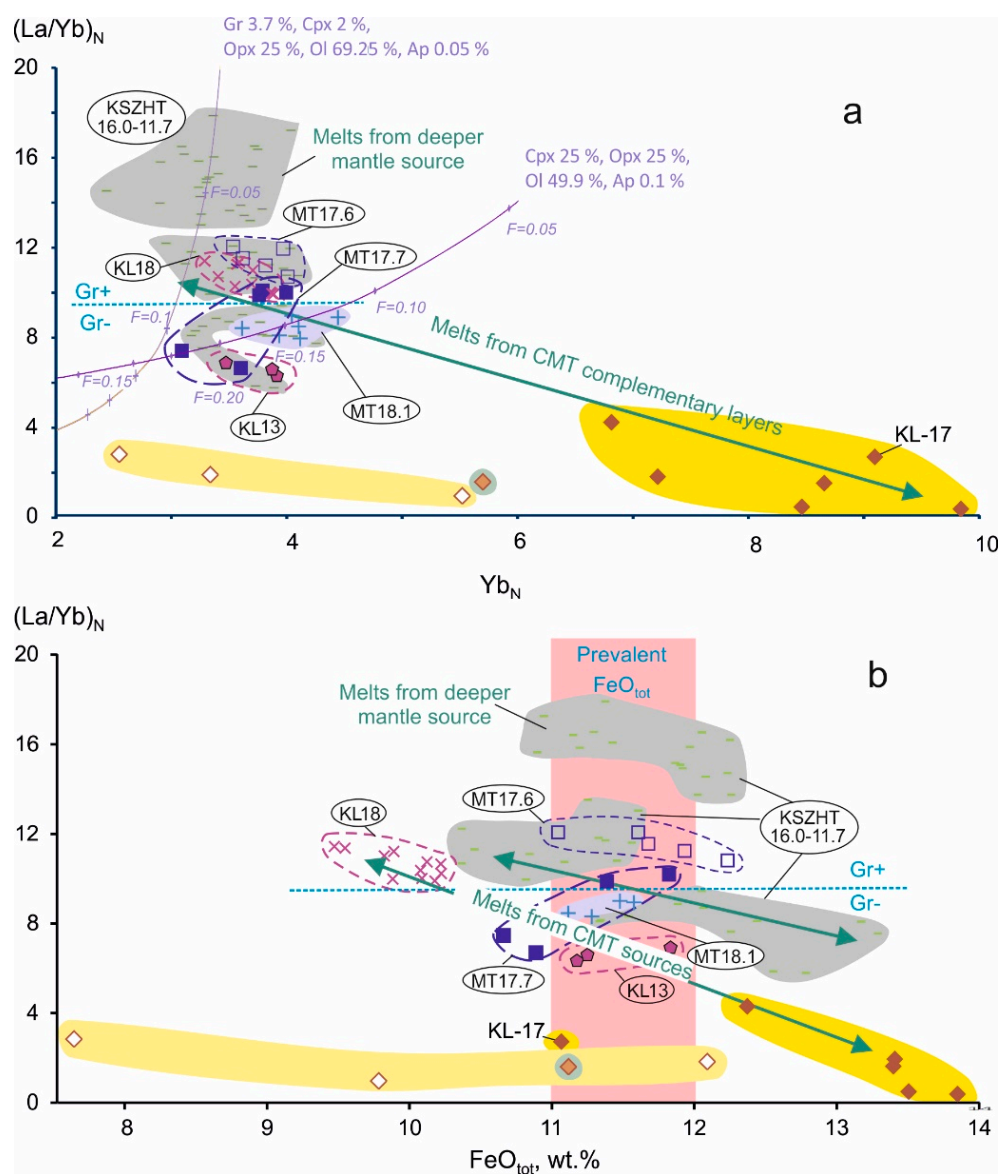


Figure 10. Cont.

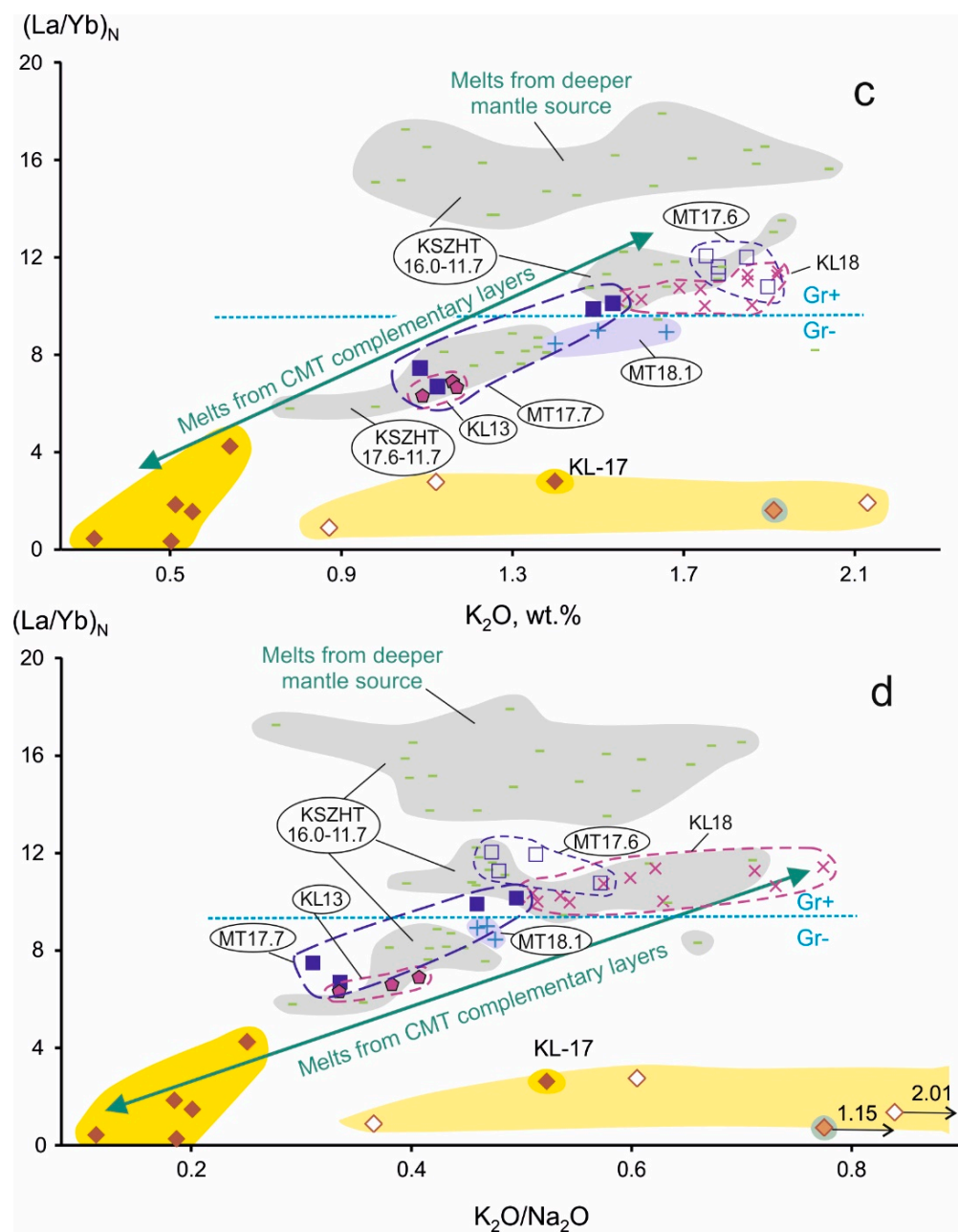


Figure 10. Comparison of the MSF basic pseudotachylytes and the KSZHT volcanic rocks on $(La/Yb)_N$ - Yb_N (a), $(La/Yb)_N$ - FeO_{tot} (b), $(La/Yb)_N$ - K_2O (c), and $(La/Yb)_N$ - K_2O/Na_2O (d) diagrams. Measured major oxide values are used. Symbols are as in Figure 9. In the Meteo Volcano, volcanic rocks of the initial eruption phase (MT18.1) belong to a garnet-free source, those of the intermediate phase (MT17.7) to both a garnet-free and a garnet-bearing deep-seated sources, and rocks of the final phase of this volcano (MT17.6) to a garnet-bearing source. In panel a, model curves of equilibrium partial melting and compositions of garnet-bearing Cpx-poor and garnet-free Cpx-rich deep-seated sources were calculated for the KSZHT volcanic rocks by Rasskazov et al. [20] using equations of [83] and mineral–melt distribution coefficients given in [84]. In panel b, prevalent FeO_{tot} interval is shown as in Figure 9b. For normalization of La/Yb and Yb , the pyrolite composition was used after [77].

On a $(La/Yb)_N$ - FeO_{tot} diagram (Figure 10b), data fields of eruptive phases MT18.1, MT17.7, KL18, and KL13 of the Meteo and Kultuk volcanoes are displaced relative to the one of the KSZHT 17.6–11.7 Ma age interval with a decrease in a $(La/Yb)_N$ ratio and with an increase in a FeO_{tot} content, denoting a composite trend that extends from the KL18 initial lava generation through phases MT18.1 and MT17.7 to the KL13 final lava generation and moderate-Ti basic pseudotachylytes. Consequently, in terms of a FeO_{tot} content, the garnet-free source of the MSF moderate-Ti pseudotachylytes was complementary to the garnet-bearing source that generated lavas of the Kultuk Volcano. Taking into account local occurrence of these complementary deep-seated sources in the MSF, one can assume that a deep-seated lava source of the Kultuk Volcano was depleted in iron as a result of its removal from the garnet-bearing sub-crustal lithospheric mantle and its transfer to the crustal level. These additional portions were reflected in generation of moderate-Ti pseudotachylytes. Any complementary links between deep-seated sources of low-Ti pseudotachylytes and those of volcanic rocks are doubtful.

The KSZHT lavas erupted on the area between the Kultuk and Meteo volcanoes show a parallel complementary trend of rocks from garnet-bearing and garnet-free deep-seated sources, shifted to the right and above the one of the Kultuk and Meteo volcanoes. The mantle (garnet-bearing) and crustal (garnet-free) sources of this trend yield higher FeO_{tot} content than KL13, which corresponds to the prevailing FeO_{tot} level. The KSZHT volcanic rocks with an elevated $(La/Yb)_N$ ratio and relatively narrow FeO_{tot} range are also distinguished as low-degrees derivatives of the garnet-bearing mantle source.

On $(La/Yb)_N$ - K_2O and $(La/Yb)_N$ - K_2O/Na_2O diagrams (Figure 10c,d), volcanic rocks of the eruptive phases MT18.1, MT17.7, KL18, and KL13 from the Meteo and Kultuk volcanoes form trends almost coincided with those of rocks from other KSZHT volcanoes. These diagrams demonstrate an increasing role of a K_2O in melts from garnet-bearing deep-seated sources with its complementary decreasing in those from garnet-free ones.

6.3. Ce/Pb Ratio

Sample KL-9 has a Ce/Pb ratio close to that in the undifferentiated mantle. In other samples of the moderate-Ti pseudotachylyte group, a Ce/Pb ratio decreases to values of the continental crust. The low-Ti pseudotachylyte group shows a Ce/Pb ratio in a range of typical lower crustal compositions.

On TiO_2 -Ce/Pb and MgO-Ce/Pb diagrams (Figure 11a,b), sample KL-9 fits to lava trends of the first two phases in the Meteo Volcano (MT18.1 and MT17.7). Rocks of the initial eruption phase in the Kultuk Volcano (KL18) also partially fall into this trend. On the MgO-Ce/Pb diagram, rocks from this volcano are mostly shifted to the left with decreasing Ce/Pb ratio. In lavas of other KSZHT volcanoes, a Ce/Pb ratio increases to the ocean basalt value and partially exceeds it.

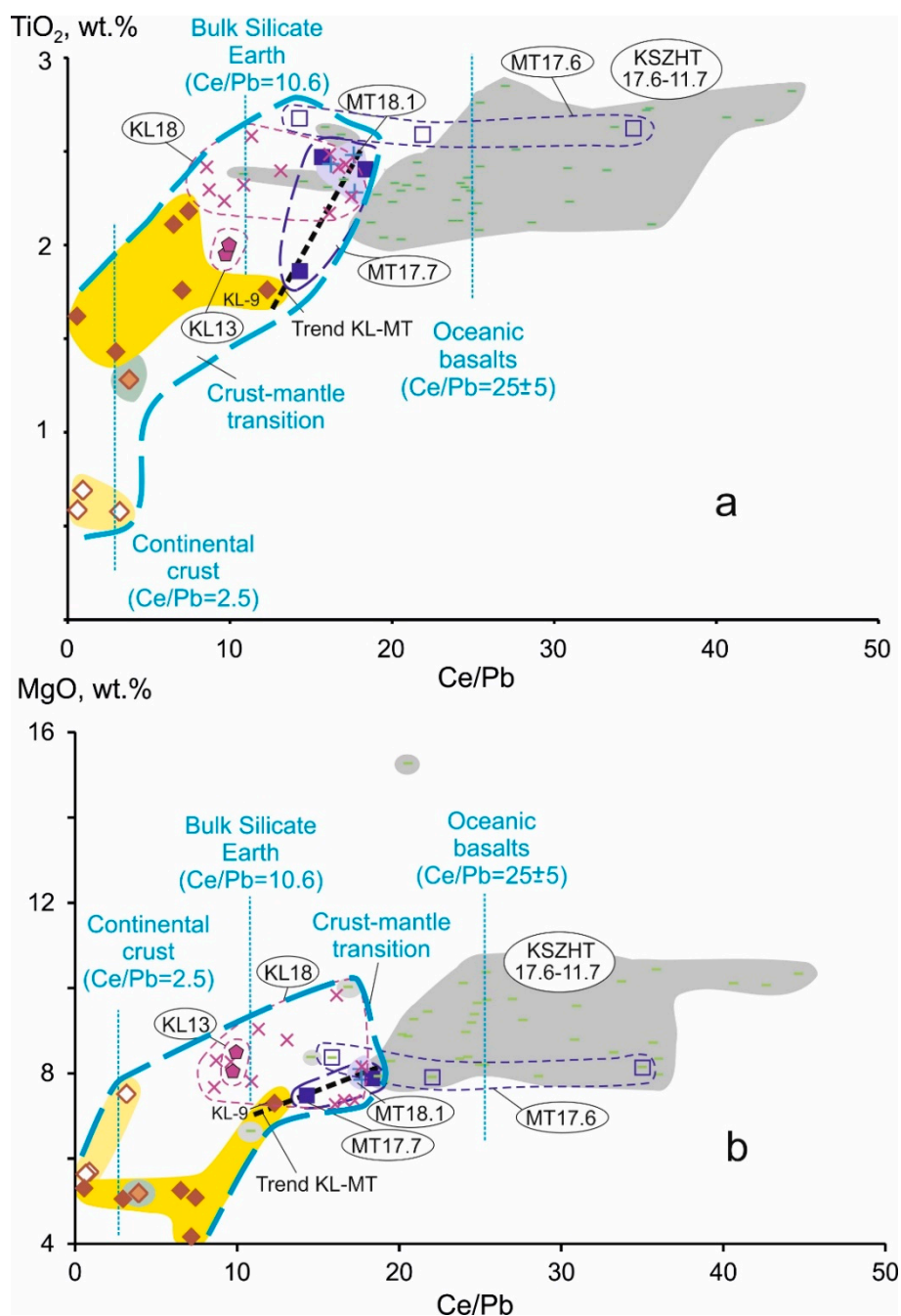


Figure 11. Comparison of basic pseudotachylytes from the MSF and volcanic rocks from the KSZHT on TiO_2 -Ce/Pb (a) and MgO-Ce/Pb (b) diagrams. Measured major oxide values are plotted. Designated as KL–MT are the common trends of pseudotachylyte KL-9 and lavas from the first two phases of the Meteo Volcano (MT18.1 and MT17.7). The Ce/Pb values for ocean basalts and continental crust are shown after [85], the Bulk Silicate Earth value is after [86]. Symbols are as in Figure 9.

6.4. Th/Yb and Ta/Yb Ratios

On the Th/Yb versus Ta/Yb diagram, rocks of the continental crust are plotted above the mantle array displayed by OIB and MORB [87]. In a garnet-bearing source, both ratios increase; while in absence of garnet, both ratios decrease. Points of initial lavas from a garnet-free source of the Meteo Volcano (MT18.1) are shifted below the ocean basalt array with a relative increase in a Ta/Yb ratio (Figure 12a). Points of lavas of the next eruption phase from a garnet-free source of the same volcano (MT17.7) are slightly shifted relative the data field of initial lavas toward the lower crust composition. A more advanced shift

is shown by final basalts from the garnet-free source of the Kultuk Volcano (KL13), while lavas of the initial eruptions of this volcano (KL18) belong to a trend of garnet-bearing deep-seated sources that extends along the OIB and MORB array. Melts from the KSZHT deep-seated sources are complementary enriched in tantalum (with increasing Ta/Yb and decreasing Th/Ta) relative to OIB melts due to melting both garnet-free lower crust and underlying garnet-bearing mantle. Melts of basic pseudotachylytes from the garnet-free crust, on the contrary, are complementary depleted in tantalum (with a relative decrease in Ta/Yb) (Figure 12b). The KSZHT magmas erupted from sources of modified restite material that had lost the basic pseudotachylyte component.

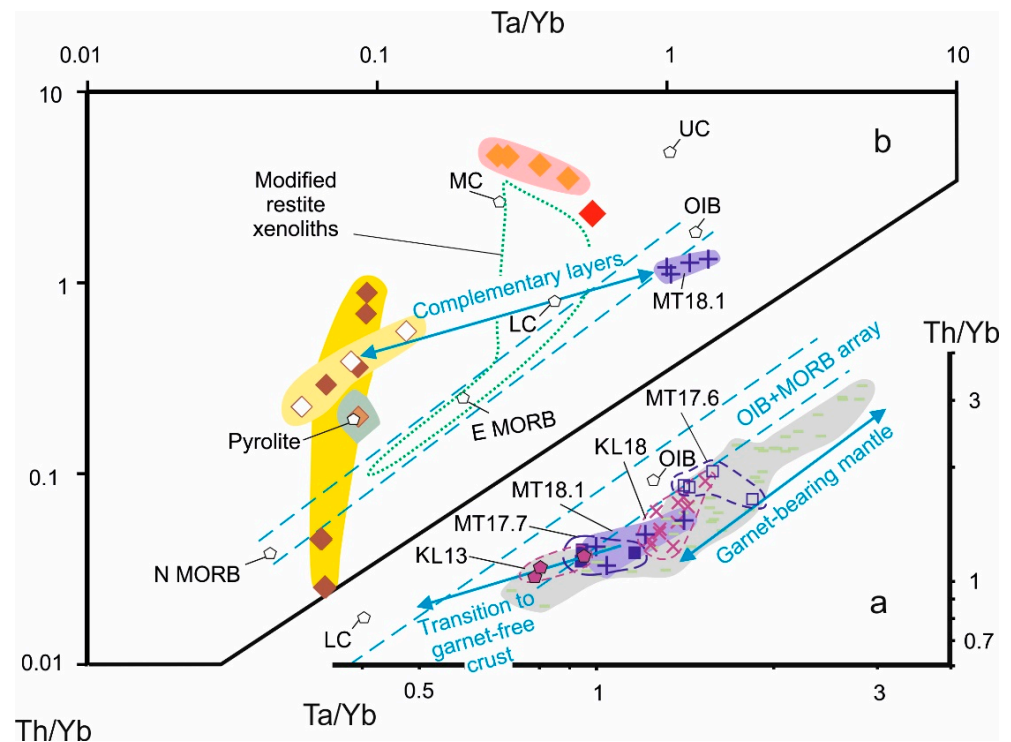


Figure 12. Th/Yb-Ta/Yb diagrams of the initial basalts from the Meteo Volcano erupted about 18.1 Ma (MT18.1) in comparison with other volcanic rocks from the KSZHT (a) and with pseudotachylytes from the MSF (b). On the diagram b, a data field of peridotite nodules from trachybasalts of the Karerny volcano is shown as a possible source of the KSZHT melts after [60]. Additional abbreviations: N MORB and E MORB—normal and enriched basalts of the mid-ocean ridge, respectively [88], LC, MC, and UC—lower, middle, and upper crust, respectively [89]. Symbols are as in Figure 9.

In the MSF, pseudotachylytes of intermediate and silicic compositions are also associated with sources of the collisional crust. On the Th/Yb–Ta/Yb diagram (Figure 12a), points of these pseudotachylytes correspond to the end of a trend exhibited by crustal xenolith. The trend extends from the ocean basalt array to the middle crust composition. A common nature of intermediate and silicic pseudotachylyte compositions is emphasized by similar REE patterns (Figure 7a). At the same time, the middle crust differs from its lower part by oxidation conditions and occurrence of water-bearing mineral phases. This is characteristic of the source for pseudotachylytes of intermediate composition that lost uranium with notably increased Th/U ratio (Figure 6).

6.5. Sr and Nd Isotope Ratios

On a $^{143}\text{Nd}/^{144}\text{Nd}$ – $^{87}\text{Sr}/^{86}\text{Sr}$ diagram (Figure 13), a particular role of a garnet-free source for initial basalts from the Meteo Volcano is highlighted. Compared with the entire set of the KSZHT volcanic rocks, lavas of the MT18.1 eruption phase yield a separate group with the lowest $^{143}\text{Nd}/^{144}\text{Nd}$ and highest $^{87}\text{Sr}/^{86}\text{Sr}$ isotope ratios. The 17.7 Ma

lavas from the Meteo Volcano show notable decrease in $^{87}\text{Sr}/^{86}\text{Sr}$ ratio at $^{143}\text{Nd}/^{144}\text{Nd}$ ratio comparable to that of the initial (18.1 Ma) basalts and partly exceeding it. Lavas of the 17.6 Ma phase show limited variations of Nd and Sr isotope ratios within their ranges corresponded to those of the previous eruption phase. At the same time, data points of the 17.6 Ma lavas start the 16.0–11.7 Ma KSZHT array of increasing $^{143}\text{Nd}/^{144}\text{Nd}$ and decreasing $^{87}\text{Sr}/^{86}\text{Sr}$ ratios.

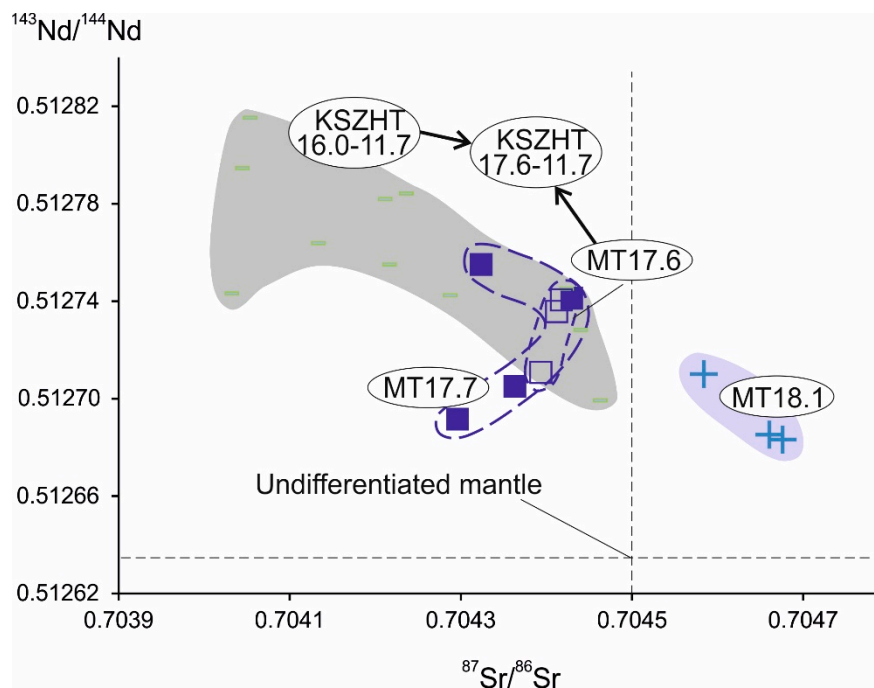


Figure 13. $^{143}\text{Nd}/^{144}\text{Nd}$ – $^{87}\text{Sr}/^{86}\text{Sr}$ diagram showing points of the initial eruption phase from a garnet-free source (MT18.1) in the Meteo Volcano, the intermediate phase from the garnet-free and garnet-bearing sources (MT17.7), and the final phase of this volcano (MT17.6). The latter is comprised with a set of younger volcanic rocks from garnet-free and garnet-bearing sources (KSZHT16.0–11.7) into a common array (KSZHT 17.6–11.7). Symbols are as in Figure 9.

6.6. Pb Isotope, Nb/U, and Th/U Ratios

A diagram of $^{207}\text{Pb}/^{204}\text{Pb}$ plotted versus $^{206}\text{Pb}/^{204}\text{Pb}$ incorporates only data on uraniumogenic Pb isotopes and yields timing of convective homogenization and modification of a source material. A diagram of $^{208}\text{Pb}/^{204}\text{Pb}$ plotted versus $^{206}\text{Pb}/^{204}\text{Pb}$ shows relationship between thorogenic ^{208}Pb and uraniumogenic ^{206}Pb . The former is a final decay product of the ^{232}Th series, the latter is a final one of a ^{238}U series that makes up 99.2743% of a total mass of uranium [90]. Consequently, distribution of points on the $^{208}\text{Pb}/^{204}\text{Pb}$ – $^{206}\text{Pb}/^{204}\text{Pb}$ diagram designates variations of a time-integrated $^{232}\text{Th}/^{238}\text{U}$ ratio as a factor of the element concentrations. In ocean basalts, Th and U belong to a group of geochemically similar incompatible elements: $\text{Th} > \text{U} \sim \text{Nb}$ [88]. Melts derived from mantle and crustal sources reveal markedly different Nb/U ratios: 47 ± 10 in OIB and ~ 10 in crust-derived volcanic rocks [85,91]. The Th/U value ~ 4 in mantle rocks increases to 6 in lower crustal ones [89]. This ratio may vary because of different garnet–melt and/or clinopyroxene–melt partitioning of U and Th [92,93]. Anomalously high or low Th/U values can also be related to input or removal of U, migrated under oxidizing conditions due to the formation of water-soluble uranyl UO_2^{2+} compounds with hexavalent U.

On diagrams of Pb isotope ratios (Figure 14a,b), the KSZHT volcanic rocks are plotted both as slightly scattered fields and as discrete points. In Figure 14a, a bending array extends from the point of $^{207}\text{Pb}/^{204}\text{Pb} = 15.40$ and $^{206}\text{Pb}/^{204}\text{Pb} = 17.28$ to the one of $^{207}\text{Pb}/^{204}\text{Pb} = 15.52$ and $^{206}\text{Pb}/^{204}\text{Pb} = 18.2$. The lower and middle parts of the array show

older source linearity directed at the Inner Asia common mantle component referred to as episodically raised uniform deep mantle material [94]. Points of a lava subgroup from the Kultuk Volcano, designated as KL18', yield a line with a slope corresponding to an age of about 2.22 Ga. The line relation to the Inner Asia common component assumes the initial source generation at that time. Points, shifted to the right and to the left in the middle and upper parts of the array, indicate its distortion. A lava subgroup KL18'' designates a source processing, approximated with a line with a slope corresponding to an age of about 0.9 Ga. Separate data fields of the MT18.1 and MT17.7 eruptive phases assume a slope of points close to the 2.22 Ga array (or steeper than this), indicating coeval or older differentiation of a source material, while a shifted data field of the 17.6 Ma eruptive phase clearly designates a separate source material.

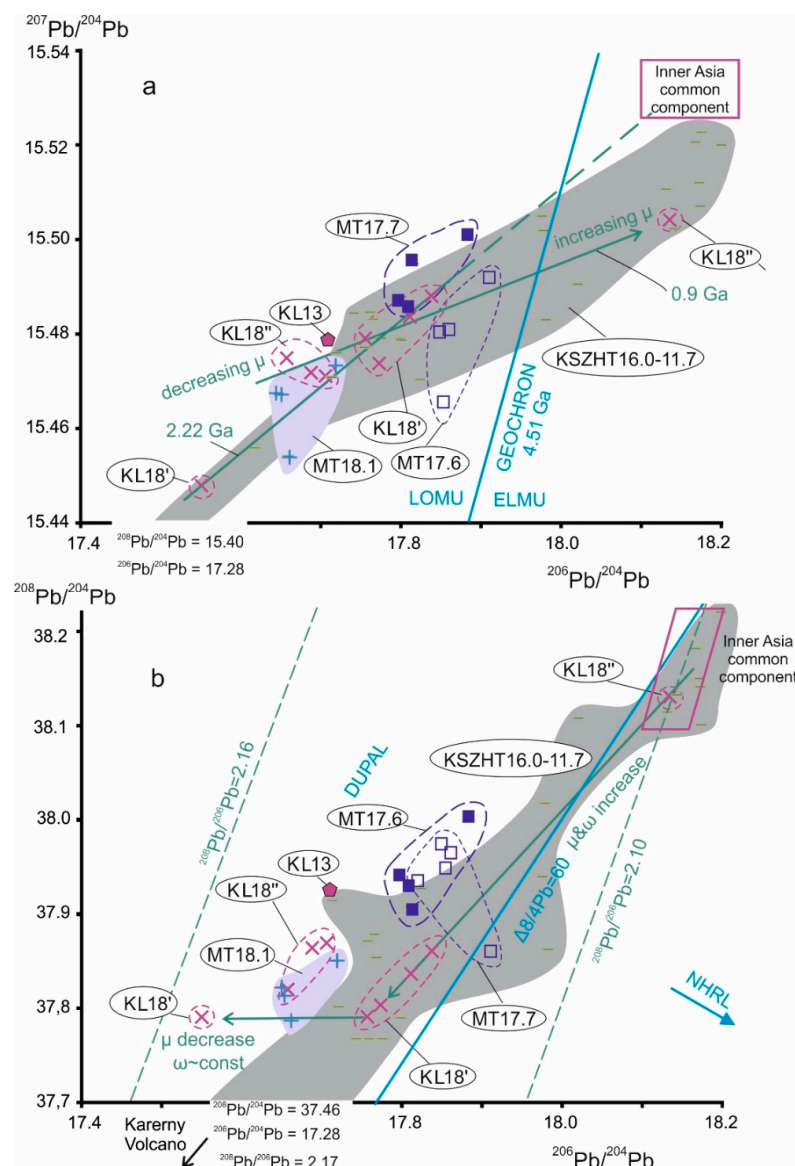


Figure 14. Diagrams of $^{207}\text{Pb}/^{204}\text{Pb}$ - $^{206}\text{Pb}/^{204}\text{Pb}$ (a) and $^{208}\text{Pb}/^{204}\text{Pb}$ - $^{206}\text{Pb}/^{204}\text{Pb}$ (b) for volcanic rocks from the KSZHT. Measurement errors of isotope ratios do not exceed icon sizes. On diagram a, shown are the Inner Asia common component and the geochron of Low μ Viscous Protomantle (LOMUVIPMA) with a slope corresponding to an age of 4.51 Ga, obtained for a source of volcanic rocks from the northwestern Udokan volcanic field in the reactivated part of the Siberian paleocontinent [94]. On diagram b, designated are the boundary of the DUPAL anomaly at $\Delta 8/4\text{Pb} = 60$ [95] and estimated maximal $^{232}\text{Th}/^{238}\text{U}$ ratio (explanation in the text). Symbols are as in Figure 9.

On a diagram of thorogenic and uraniumogenic Pb isotope ratios (Figure 14b), four points of the KL18' subgroup (source age of 2.2 Ga) show well correlated $^{238}\text{U}/^{204}\text{Pb}$ (μ) and $^{232}\text{Th}/^{204}\text{Pb}$ (ω) ratios. The only point of this subgroup, shifted to the left, indicates decreasing μ without changing ω . The KL18'' subgroup (source age of 0.9 Ga) shows one point fitted to the KL18' correlation line and three points shifted to the left. On the one hand, increasing μ and ω values result in transition from the DUPAL to non-DUPAL signature, on the other hand, ω values do not vary under decreasing μ . Three phases of the Meteo Volcano show data points generally shifted to the left of the 2.2 Ma KL18' array of consistently varied μ and ω (but one point) and extend along the KL18'' array of a source region affected by decreasing μ without changing ω .

On Figure 14b, the most radiogenic leads of the KSZHT volcanic rocks correspond to the Inner Asia common component. From this relationship, Pb isotope data can be used for estimation of a Th/U ratio in a source region. Since the common component represents the uniform deep-mantle material [94], the array of Figure 14b characterizes a differentiation event of 2.22 Ga. A ^{232}Th has a longer half-life than a ^{238}U (14.010×10^9 years versus 4.468×10^9 years) [90]. Hence, a ^{238}U produces more of ^{206}Pb than a ^{232}Th generates of ^{208}Pb in the same period of time. The Inner Asia common component yields the $^{208}\text{Pb}/^{206}\text{Pb}$ value of 2.10 that can correspond to the initial $^{232}\text{Th}/^{238}\text{U}$ ratio as high as 6.58. Respectively, radioactive decays of ^{232}Th and ^{238}U can result in increasing $^{232}\text{Th}/^{238}\text{U}$ ratio from 6.58 up to 20.6. This value is the upper limit of the present-day Th/U ratio.

The CMT deep-seated sources of the KSZHT volcanic rocks show significant deviations of Nb/U and Th/U ratios from the OIB values. On diagrams of Figure 15a,b, rare points are notably shifted to the right. Due to increased partial melting, the $(\text{La}/\text{Yb})_{\text{N}}$ values in the left clusters of points are slightly decreased. Predominating data points with low Nb/U and Th/U ratios may indicate intensive magma generation processes in U-rich sources that are characteristic of both garnet-bearing and garnet-free layers of the CMT region.

A Nb/U ratio reveals a distinct contrast between melt generations in initial deep-seated sources of the Kultuk and Meteo volcanoes; in the KL18 lavas from a garnet-bearing source of the former, the Nb/U ratio decreases (to 25) and in the MT18.1 lavas from the garnet-free source of the latter, on the contrary, increases (to 110). A similar contrast between the initial KL18 and MT18.1 lavas is displayed in the Th and U distributions; in the KL18 lavas from the garnet-bearing source of the Kultuk Volcano, the Th/U ratio decreases (to 1.8), while in the MT18.1 lavas from the garnet-free source of the Meteo Volcano, on the contrary, it increases (to 8). During the initial KL18 phase of the Kultuk Volcano, only the melts from a garnet-bearing source, enriched in uranium, took place. Displayed at the end of the KSZHT activities was a material of a garnet-free source of the Kultuk Volcano that, in terms of Th/U and Nb/U ratios, was partly similar to the one of the MT17.7 phase of the Meteo Volcano.

The KSZHT volcanic rocks from the deeper lithospheric mantle source show mainly Th/U ratio less than 4 with rare samples exceeded this value (Figure 15b), although data points of this group demonstrate almost symmetrical distribution relative to the OIB average Nb/U ratio (~47) (Figure 13). This difference indicates better sensitivity of a Th/U ratio than a Nb/U one to U-redistribution in a source region due to a Th abundance in volcanic rocks 1–2 orders of magnitude lower than a Nb one.

In contrast to the KSZHT volcanic rocks, the MSF basic pseudotachylytes show inconsistent variations of Nb/U and Th/U ratios. The Nb/U one in depleted rocks ($(\text{La}/\text{Yb})_{\text{N}} < 1$) approaches the ocean basalt value, decreasing to crustal one in rocks with chondritic slightly enriched REE distributions ($(\text{La}/\text{Yb})_{\text{N}} = 1.2\text{--}4.4$). The Th/U ratio in the depleted rocks differs significantly from that of ocean basalts, overlapping the entire Th/U range of basic pseudotachylytes from 2.5 (MORB) to 6.0 (lower crust). Taking into account the better sensitivity of the Th/U ratio to uranium transfer, its low values in basic pseudotachylytes may be explained by local fluid enrichment in uranium of a source, similar to the ratio in the CMT deep-seated sources of volcanic rocks.

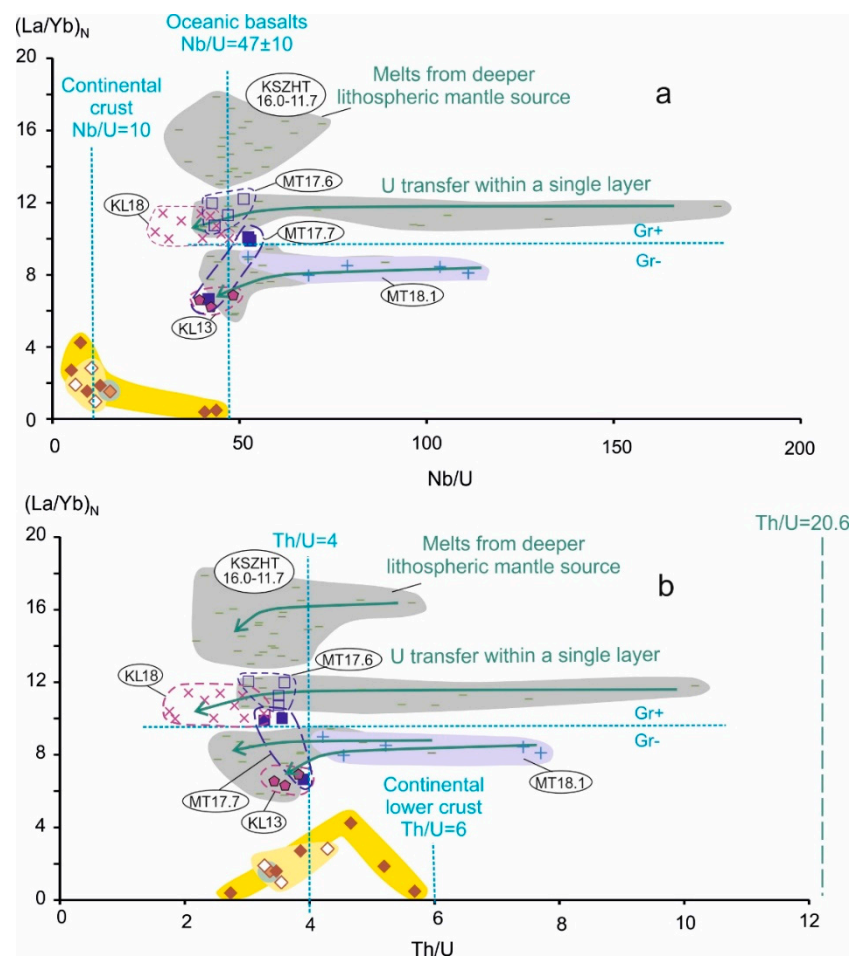


Figure 15. Comparison of basic pseudotachylytes from the MSF and volcanic rocks from the KSZHT on $(La/Yb)_N$ -Th/U (a) and $(La/Yb)_N$ -Nb/U (b) diagrams. Symbols are as in Figure 9. Green arrows indicate extraction of U from layers by oxidized fluids that result in decrease of $(La/Yb)_N$ due to locally increasing degrees of melting. The upper Th/U limit of 20.6 is shown for a source region from Pb isotope data. $(La/Yb)_N$ is calculated using the pyrolite composition after [77].

7. Discussion

7.1. Long-Term CMT Evolution

On the one hand, volcanic rocks of the initial and final eruption phases in the Meteo and Kultuk volcanoes yield common trends with basic pseudotachylytes (Figures 8–10) that assumes searching for genetic relationships between the rock sources with a perspective of creating a comprehensive model for the development of seismotectonic processes in the crust and sub-crustal mantle of the Slyudyanka paleocollision zone, inherited by the South Baikal Basin and Tunka Valley. On the other hand, clearly expressed is the iron redistribution with its removal from the CMT garnet-bearing source of the KL18 lavas in the Kultuk Volcano to the crustal source of the MSF basic pseudotachylytes. From complementarily redistributed Fe, U, and alkalis in deep-seated sources of the KSZHT volcanic rocks, the CMT processes are related to episodes from about 2.22 Ga and 0.9 Ga (Figure 14a).

The basement of the southern edge of the Siberian paleocontinent, accessible for observations, has a protolith age of 3.82 Ga estimated from the conjugated Holmes-Houtermans and Wasserburg model for J-type ore leads with μ as high as 20.1 [10]. The obtained Pb age estimate of the protolith is comparable with the Nd model age limit of 3.9 Ga for the Archean metamorphic rocks from the Irkutsk block of the paleocontinent [96].

The Baikal granulite–gneiss terrane of the Irkutsk block was affected by collisional metamorphic events, dated by the U–Pb zircon method from about 2.8 Ga, 2.65–2.56 Ga, and 1.866–1.853 Ga. The Archean metamorphic episodes were designated in rocks of granulite facies, and the Early Proterozoic one in those of high-temperature amphibolite and partially granulite facies [97]. In addition, metamorphic events were recorded using the Rb–Sr isotope system. In the Onot greenstone belt, migmatites and granites of the basement are constrained between 2.64 and 2.24 Ga [98]. This interval also is shown by an age of 2.45 ± 0.38 Ma obtained for phlogopitization of the Krutaya Guba komatiite-like bodies [99]. These events were concurrent with the initial CMT complementary Fe–U–alkaline processes related to the Inner Asia common component.

The model calculations show that ore leads were extracted from crystalline rocks in time intervals from 1.8–1.5 Ga, 1.2–0.9 Ga, 0.6–0.5 Ga, and about 0.25 Ga [10]. The first episode of the Pb extraction in ore deposits began after the Siberian paleocontinent assembly, accompanied by A-type granite magmatism of the Primorsky complex from about 1.86 Ga [100–103]. The end of the second episode coincided with the CMT complementary Fe–U–alkaline processes. Two other episodes are also connected with tectonic and magmatic events spotted in the accessible crust.

The remarkable one is displayed along the southern edge of the Siberian paleocontinent in the Late Precambrian alkaline–ultrabasic magmatism with carbonatites [104,105]. Syn-collisional granulite metamorphism of the Slyudyanka Group is constrained by U–Pb zircon ages of 488.5 ± 0.6 Ma and 488.0 ± 0.5 Ma obtained for hypersthene-bearing biotite and two-pyroxene trondhjemites. Post-collisional gabbro–syenite magmatism is dated at 471 ± 2 Ma [106]. The latter age is consistent with the Rb–Sr one of 470 ± 25 Ma, obtained for syenites and related rocks of the Bystraya massif with an initial $^{87}\text{Sr}/^{86}\text{Sr}$ ratio of 0.7047 ± 0.0007 [107]. Numerous small bodies and relatively large gabbro–syenite massifs (Snezhnaya, Bystraya, and Bezymyany), cut through metamorphic rocks of the Slyudyanka paleocollision zone, are compositionally similar to basic pseudotachylytes from the MSF. A TiO_2 content of these rocks varies from 0.5 to 3.0 wt% [108].

In the Mesozoic, sufficient iron redistribution provided formation of phoscorite ore deposits in the Angara Province associated with alkaline carbonatite magmatism in the southern edge of the Siberian paleocontinent [109] that affected also accreted terranes [110,111].

7.2. U in CMT Processes

In terms of Pb isotope ratios, the KSZHT deep-seated magma sources show high Th/U ratio of the Inner Asia common material raised from the deep mantle in the Paleoproterozoic (Section 6.5). This material yielded the time-integrated DUPAL anomaly. Some KSZHT volcanic rocks show the Th/U ratio as high as 10, but basically, it ranges from 2 to 4. From the discrepancy between μ and ω signatures on the Pb isotope diagrams and the Th/U ratio of the KSZHT volcanic rocks, one can assume recent fluid redistribution of U relative to Th with a preferential concentration of U in melts of the CMT deep-seated sources.

Similar to the KSZHT volcanic rocks, strongly depleted and enriched by uranium with variable Th/U and Nb/U ratios with respect to the OIB values are Miocene lavas from the Primorye and Lesser Khingan and also Cretaceous–Paleogene lavas from the Tien Shan (Figure 16). The Th/U ratio as high as 20 is characteristic of basalts and trachybasalts derived from the CMT garnet-free source in the Nakhodka volcanic field of the Primorye, Far East of the Russia. Associated with these rocks basaltic andesites, generated in a crustal source, show also elevated Th/U ratio (up to 10). The lower limit of the Th/U ratio in volcanic rocks from this area is 4 [9].

Uranium depletion with a Th/U ratio as high as 15.5 is characteristic of basanites and associated rocks from a garnet-free CMT source of the South Tien Shan (Tuyun Basin), in contrast to basalts and trachybasalts from a shallow (crustal) source of the Middle-North Tien Shan, which are anomalously enriched by U with a relative decrease in Th/U to 0.17. The deeper (garnet-bearing) mantle sources in the latter area do not show any signs of uranium redistribution, however. The crustal source could be enriched in uranium with

its complementary depletion of the shallow garnet-free peridotite source due to the rise of oxidized fluids through the crust–mantle boundary during the Late Paleozoic closure of the Turkestan paleocean. The Cretaceous–Paleogene disruption of the crust–mantle boundary under the South Tien Shan prevented an ascent of deeper mantle magmas and provided a long-term (122–46 Ma) generation of magmas in a shallow garnet-free peridotite source. A shielding effect of this rupture did not prevent, however, a short-term (61–53 Ma) upraise of magmas from the deeper mantle source accompanied by crustal melting in the Middle-North Tien Shan [112].

Region, area	Central BRS KSZHT	Sea of Japan Nakhodka v.f.	Tian Shan		Lesser Khingan Udurchukan v.f.
			South	Middle-North	
Crust	2.5<Th/U<6	4<Th/U<10	No erupted melts	0.17<Th/U<1.8	No erupted melts
CMT	Grt- 2.5<Th/U<8	5<Th/U<20	2<Th/U<15.5	No erupted melts	4<Th/U<16
	Grt+ 2<Th/U<10	No erupted melts	No erupted melts	OIB-like	8<Th/U<13
Deeper mantle	2<Th/U<6	No erupted melts	No erupted melts	OIB-like	OIB-like

Figure 16. Ranges of Th/U ratios in the KSZHT volcanic rocks in comparison with those from CMT deep-seated sources in other Asian regions. Data are from [9,112] and this work.

In the basalt-andesite assemblage from the Lesser Khingan, three groups of rocks are identified: (1) Moderate-K from a garnet-free source ($(La/Yb)_N = 5.3–9.8$, $Th/U = 3.7–15.9$, $Nb/U = 41–176$); (2) moderate-K from a source of garnet–spinel transition ($(La/Yb)_N = 9.7–13.4$, $Th/U = 7.9–13.2$, $Nb/U = 84–179$); and (3) high-K from a garnet-bearing source ($(La/Yb)_N = 15.7–33.5$, $Th/U = 4.6–5.9$, $Nb/U = 22–56$). Anomalous distribution of U, relative to Nb and Th, in the two former rock groups is associated with processes of uranium redistribution by oxidized fluids in the CMT, in contrast to the OIB-like relationship between these elements in the third group. This is explained by the absence of this effect in reduced conditions of a deeper mantle source. Rocks of the two former groups are found in the vast area of the Lesser Khingan, whereas those of the third one are limited only in the central part of the Udurchukan volcanic field.

From data comparisons of the selected regions (Figure 16), one can see peculiarities of the KSZHT deep-seated magma sources that show a wide range of Th/U ratios covered the entire depth interval from the crust to the deeper lithospheric mantle. In other Asian regions, wide ranges of Th/U ratio are recorded in volcanic rocks from sources of a single level (South and Middle-North Tien Shan) or two levels (Nakhodka and Udurchukan volcanic fields). A deeper lithospheric mantle material of the KSZHT volcanic rocks differs from OIB. In those from other areas, it is either absent (Nakhodka volcanic field, South Tien Shan) or indicates OIB-like signatures (Middle-North Tien Shan, Udurchukan).

7.3. CMT between South Baikal Basin and Tunka Valley

In the southern edge of the Siberian paleocontinent and adjacent Transbaikalian areas, northwesterly oriented orogenic structures change laterally to the South Baikal Rift (Figure 17a). From deep seismic sounding, the crust of the Angara-Lena tectonic step as thick as 40 km decreases to 36 km beneath the Selenga saddle that corresponds to an antecedent breakthrough of the Selenga River between the Khamardaban and Ulan-Burgasy ranges of the Sayan-Baikal Upland. Along the southwestern edge of the Siberian paleocontinent, the crust thickness increases to 54 km and reaches 60 km under the Hangay [113].

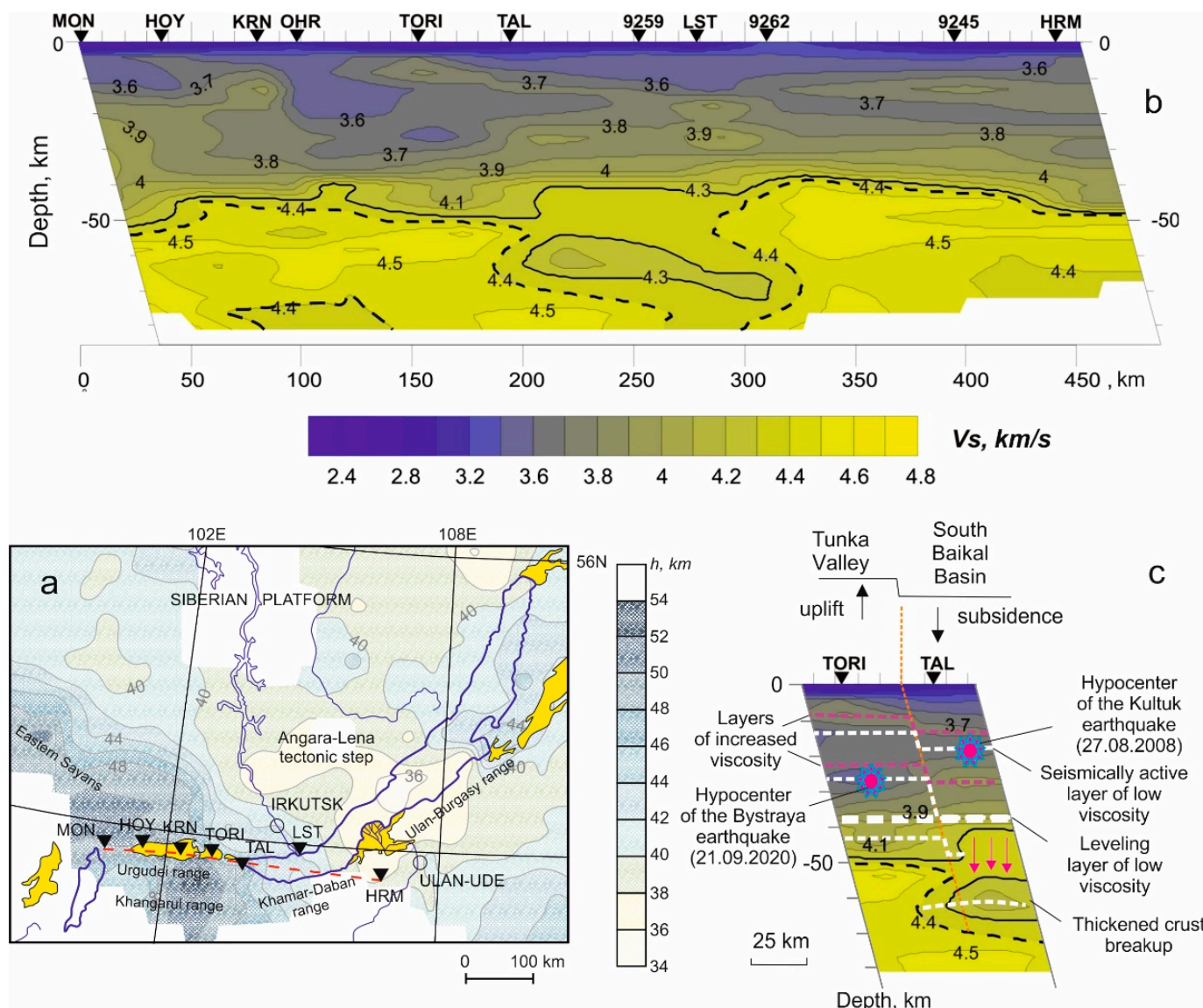


Figure 17. Map of the crustal thickness from data of deep seismic sounding (V_p) in the Baikal Rift Zone and adjacent areas of the Siberian platform and Western Transbaikal (a), V_s -section along the Mondy–Khuramsha profile (b) and a scheme of the vertical displacement of layers in the South Baikal Basin and Tunka Valley on a fragment of this section (c). On panel a, the thickness of the crust of the Angara-Lena step of the Siberian platform as thick as 36–40 km sharply increases along its southwestern edge to 54 km. Seismic tomography profile extends from an area with increased crustal thickness (Mondy) to an area with its reduced thickness under the Selenga saddle (Khuramsha). The Talaya station (TAL) approximately corresponds to the structural junction between the South Baikal Basin and Tunka Valley. The V_s isolines are plotted in steps of 0.1 km/s. Seismic drift is accounted for by the slope of the section. LST. On panel c, white dashed lines indicate vertical displacements of the low-velocity layers, burgundy dashed lines show those of the high-velocity layers (explanation in the text). The depths of the hypocenters of the 2008 Kultuk and 2020 Bystraya earthquakes (16 and 26 km) are shown after Melnikova et al. [114] and Seminsky et al. [56]. The map on panel a is modified after Mats et al. [115]. The section on panel b is adopted from Mordvinova et al. [116].

Deep seismic sounding shows decrease of P-wave velocities in the upper (sub-crustal) part of the mantle under large basins of the BRS without any decrease under inter-basin uplifts [117]. Under the South Baikal Basin, a lens of low P-wave velocities (7.7–7.8 km/s) is constrained at the mantle depths of 36–93 km. Under the central part of the Tunka Valley, a similar low-velocity lens is traced, unlike its eastern part, where a normal velocity

of 8.1 km/s is obtained, comparable to that under inter-basin uplifts. A similar relative decrease of velocities is shown in S-wave seismic tomography models [118,119].

A structure of the crust with a change in its thickness from 54 to 36 km is deciphered in the west–east V_S -section compiled along the Tunka Valley and South Baikal Basin with continuation to the southern coast of the lake (Figure 17b). From the central part of the Tunka Valley (KRN station) to the South Baikal, a dipping low-velocity zone is defined, ending at the junction between the South Baikal Basin and Tunka Valley with an abrupt lateral change in velocities under TAL station. The low-velocity crustal heterogeneity on the earth's surface corresponds to the Paleozoic granites. Under the South Baikal, a low-velocity mantle block is bounded by the V_S isoline 4.4 km/s. Low speeds are traced to a depth of at least 80 km (stations TAL–LST). Below the central Tunka Valley (KRN station), a block of reduced velocities is outlined by the S-wave velocity isoline of 4.4 km/s at a depth of more than 80 km. Between the low-velocity blocks of the central Tunka Valley and South Baikal Basins, the S-velocities increase slightly.

Late Cretaceous and Paleogene sediments and plant communities of the Prebaikal and Selenga-Vitim foredeeps were separated from each other by the South Baikal Orogen that was extended along the southeastern edge of the Siberian paleocontinent [67]. The South Baikal Basin was formed in the Neogene and Quaternary as the orogen inversion structure. Decreasing crustal thickness from the Sayan-Khamardaban mountainous region to the Selenga saddle and South Baikal Basin (Figure 17a), accompanied by abrupt lateral change of velocities at the CMT (Figure 17b), indicates recently-created geodynamic instability of the crust–mantle boundary.

The thickened Cretaceous-Paleogene crust of the South Baikal Orogen was delaminated in the Neogene and Quaternary beneath the South Baikal Basin with underplating of mantle melts. No such kind of processes occurred beneath the eastern end of the Tunka Valley. To register relative motions of deep layers at the junction between these structures, the V_S change is indicative under the TORI and TAL stations, respectively (Figure 17c). The low-velocity block is rejected under the TAL station from the base of the crust to a depth of 55–65 km with its relative thinning up to 40 km.

Between stations TORI and TAL, the structure of the middle and upper parts of the crust is generally consistent with deformations displayed on the earth's surface. Under TORI station, alternating layers with lower and higher S-wave velocities occur approximately 5 km higher than under TAL one. A vertical displacement of layers below these stations corresponds to a subsidence of the South Baikal Basin bottom relative to the uplifted end of the Tunka Valley.

From sediment distributions in the southern coast of Lake Baikal, initial subsidence of the Central Baikal area is dated back to the Eocene [120,121]. Over time, subsidence accompanied by sedimentation propagated westwards. In the Early Miocene (about 18 Ma), tectonic reactivation reached the eastern end of the Tunka Valley, providing initiation of the KSZHT volcanism, and in the Middle Miocene (about 16–15 Ma), it caused volcanism in the central part of the valley. A sharp structural reorganization at the beginning of the Pliocene led to the development of a deep basin filled by water of Lake Baikal.

Under the South Baikal basin and Tunka Valley, immediately above the region of instability at the base of the crust and in underlying mantle, a velocity of about 4.0 km/s, retained at a depth level of 37–38 km, may indicate a leveling layer of crustal and sub-crustal inhomogeneities by a through flow of low-viscosity material. This leveling layer could be generated simultaneously with differential vertical motions of the earth's surface and crustal layers beneath the South Baikal Basin and Tunka Valley. The vertical motions of the crust, associated with those in the low-viscosity layer of 37–38 km, were initiated simultaneously with magma generation in the KSZHT crust–mantle sources since ca. 18 Ma.

While assuming the main role of contrast vertical tectonic motions at the junction between the South Baikal Basin and Tunka Valley in reactivation and termination of crust–mantle magmatism in the KSZHT, it is noteworthy that the former originated due to

crustal deformations in the Primorye suture. In addition, a fragment of the paleocontinent basement was split off along the Obruchevo fault and subsided beneath the Baikal. The northeastern ruptures were stretched along the Main Sayan suture of the Siberian paleocontinent, where the KSZHT volcanism displayed during the paleocontinental block isolation along the Obruchevo fault, but became extinct after a structural disjunction between the South Baikal Basin and Tunka Valley with the subsidence of the former and uplift of the latter (Figure 18).

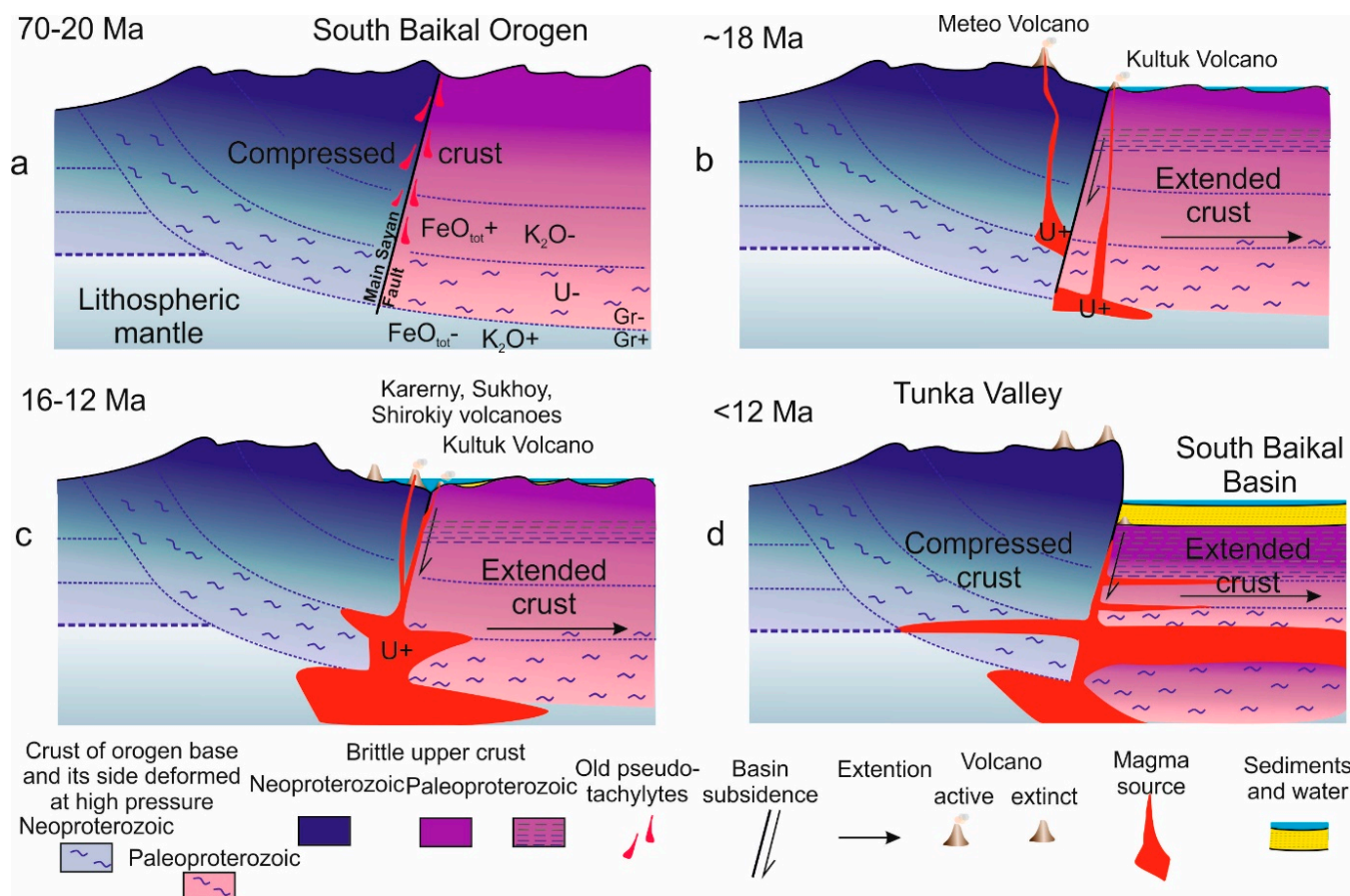


Figure 18. Generation of the CMT melts and volcanic eruptions before contrast vertical tectonic motions at the junction between the South Baikal Basin and Tunka Valley (explanations in the text).

Numerical simulations [122] indicate a dependence of magma intrusion on tectonic forces applied to the lithosphere and/or heat flow recorded on the earth’s surface. Extensional forces are usually concentrated along a rheological boundary, so a lateral propagation of a fracture leads to intrusion of magmatic melts along it. Such control takes place in case of a significant application of tectonic stress to the lithosphere ($>10^{11}$ N/m). At a relatively low heat flux (<80 mW/m²), the Moho boundary acts as a trap for rising mantle melts, while in case of a high heat flux (>80 mW/m²), a stress in the mantle weakens, so the melts rise unhindered. The reported in our study control of U enrichment by oxidized fluids with progressed magma generation in the CMT layered structure suggests a propagation of low-viscosity layer at the depth of 37–38 km from the South Baikal Basin to the adjacent Tunka Valley that caused the cessation of ascends and eruptions of the KSZHT magmatic melts about 12 Ma. The volcanism extinction signified a temporal transition from effective hot transension of the crust and underlying mantle to strict control of magmas by the CMT layered structure.

7.4. Structural Control of Strong Earthquakes

The South Baikal Basin is infilled with sedimentary layers as thick as 4 km, lying on a seismically isotropic basement [70]. At depths of 6–14 km, the velocity section shows, however, a layer-like structure that was presumably interpreted by Suvorov and Mishen'kina [123] as Mesozoic and Paleozoic sedimentary units. Such interpretation contradicts a composition of the South Baikal oil, derived from a source with land angiosperm plants that cannot be older than Cretaceous [124]. In addition, the granulite metamorphic zone, recorded along the southern coast of Lake Baikal [73], suggests the MSF extension under the South Baikal from the Kultuk village to the Tankhoi tectonic step. Therefore, the layer-like structure of the middle and upper crust could result from seismogenic sub-horizontal tectonic move apart displacements at the suture zone of the Siberian paleocontinent.

In an area between Lake Baikal and Oka River (Eastern Sayans), the MSF plane dips to the southwest (angle 60–70°) with sub-vertical fragments [53,125,126]. Similar inclination of the MSF plane is reconstructed in the eastern part of the Tunka Valley from fractures in mylonites (Figure 3) and is displayed in a nodal plane of the 2020 Bystraya earthquake mechanism solution. The latter coincides with the dip of a nodal plane obtained for the 2008 Kultuk earthquake, the epicenter of which was in the Baikal area (i.e., in the east-southeastern continuation of the MSF, about 40 km from the Kultuk village) (Figure 19). Consequently, the Main Sayan suture zone played a major role in generating pseudotachylytes, the KSZHT volcanic rocks, and modern seismogenic deformations both in the South Baikal basin and in the adjacent Tunka Valley.

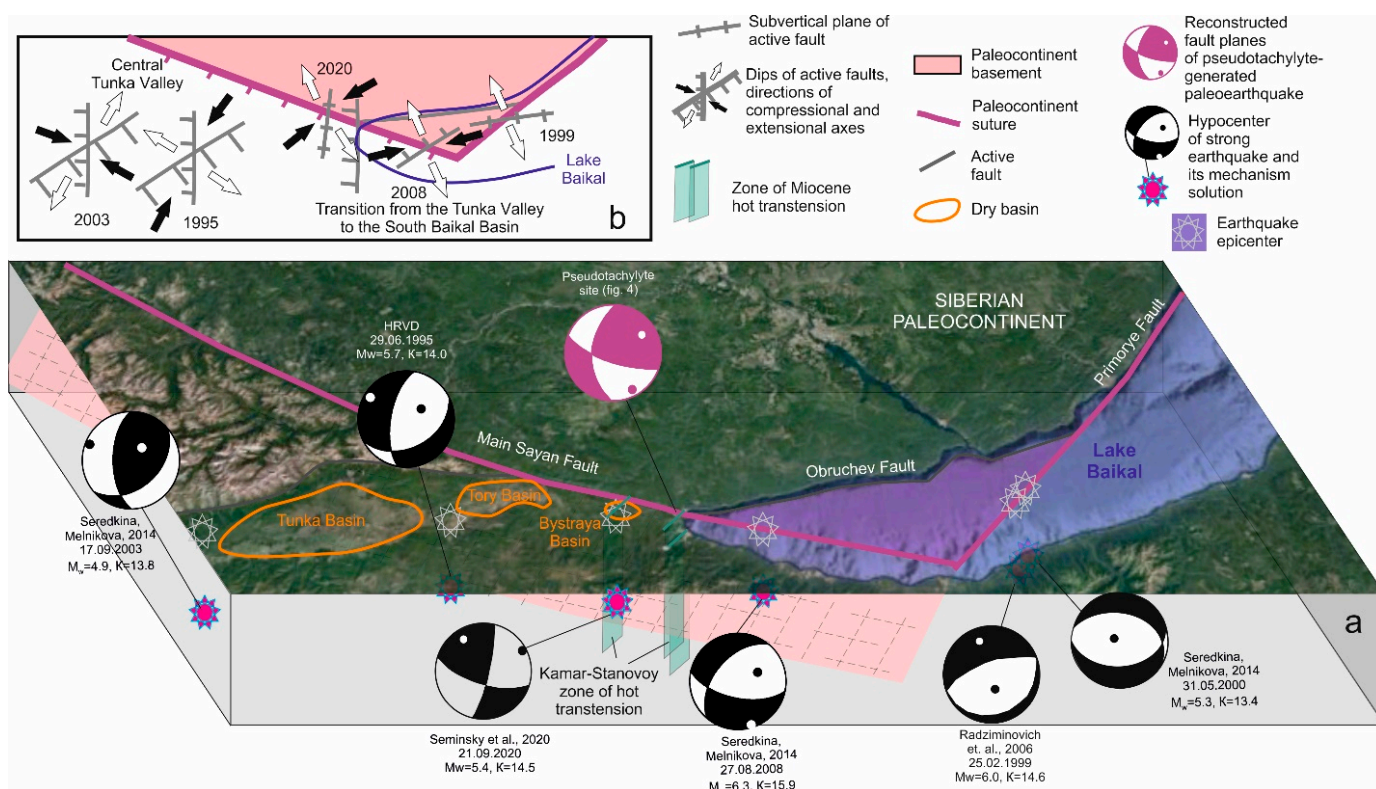


Figure 19. Schematic block-diagram of the Tunka Valley and South Baikal Basin for comparison between the fault planes Scheme 3. and the nodal planes, reconstructed from focal mechanism solutions of earthquakes in seismically active faults (a) and schematic change in compression and extension forces in active faults of the Tunka Valley and South Baikal Basin (b). Focal mechanism solutions of strong earthquakes are shown after [56,127–129].

In the present-day structural development of the central BRS, elastic stresses accumulate with strong seismic shocks along the Primorye and Main Sayan suture boundaries

of the Siberian paleocontinent. Along strike changes are displayed in both directions of the earth's surface motions, recorded by GPS geodesy, and earthquake mechanism solutions [56,130]. Deformations of the Primorye suture were implemented in the South Baikal earthquake on February 25, 1999 ($M_w = 6.0$). In a focal zone, a transverse rupture was reactivated, parallel to the Obruchev fault, with sub-vertical and sub-horizontal positions of the nodal planes. This indicates a control of extension by a sub-horizontal low-viscosity layer. The weaker aftershock on May 31, 2000 ($M_w = 5.3$) had a normal fault mechanism of slightly tilted nodal planes. In a seismic shock of the Kultuk earthquake on 27 August 2008 ($M_w = 6.3$) of the subsided (Baikal) part of the Main Sayan suture, a strike-slip mechanism of displacement of the transverse to it (northeastern) rupture, parallel to the Primorye suture, was implemented. In the 2020 Bystraya earthquake, lateral displacements occurred in the uplifted (Tunka) part of the Main Sayan suture. The general northeastern extension of the crust was preserved both in the South Baikal Basin and in the adjacent eastern part of the Tunka Valley.

During seismic reactivations of 2003–2017, epicentral fields of earthquakes in the South Baikal Basin were spatially separated from those in the Tunka Valley by an aseismic area. Similarly distributed, but small, seismic events occurred in the 1995–1999 time interval before the strong South Baikal earthquake on February 25, 1999 ($M_w = 6.0$) [55]. The 2020 Bystraya earthquake was spatially related to the MSF reactivated in the eastern part of the Tunka Valley and spatially coincided with the Anchuk volcano of the Bystraya volcanic zone in the KSZHT (Figure 1).

Seismogenic crustal deformations in the central part of the Tunka Valley differ from those in its eastern part. The 1995 Zaktui and 2003 Khoytolog earthquakes took place to the east and to the west of the Tunka basin, respectively, with focal mechanism solutions showing opposite propagations of compressional and extensional waves.

The 2008 Kultuk earthquake focus as deep as 16 km corresponded to a low-velocity layer (Figure 17c). The seismic activity reflected its low viscosity. The deeper crustal leveling layer of 37–38 km is aseismic, but the one of 25–27 km with reduced velocities corresponded to the 2020 Bystraya earthquake. This low-viscosity seismically active layer is located under the Tunka Valley deeper than the one of the South Baikal Basin. Seismogenic deformations of this earthquake could be transferred to the underlying leveling layer of 37–38 km and trigger motions along it in the entire central part of the BRS. This sequence explains why the main earthquakes of seismic reactivations in the South Baikal water area are preceded by seismic events of the Kultuk area.

7.5. Geodynamic Control of CMT Magmatism

On a Th/Yb versus Ta/Yb plot, points of andesites and trachyandesites from the East Hangay Orogen correspond to a lower crustal source above the OIB and MORB array and basalts show a trend extended below this array [19]. A trend of volcanic rocks from the Orkhon-Selenga saddle is shifted below the OIB and MORB array, similar to the one of the KSZHT volcanic rocks shown in Figure 12. Both in the Tunka Valley and in Central Mongolia, the CMT signatures of volcanic rocks change to the OIB-type ones westward (Figure 20a).

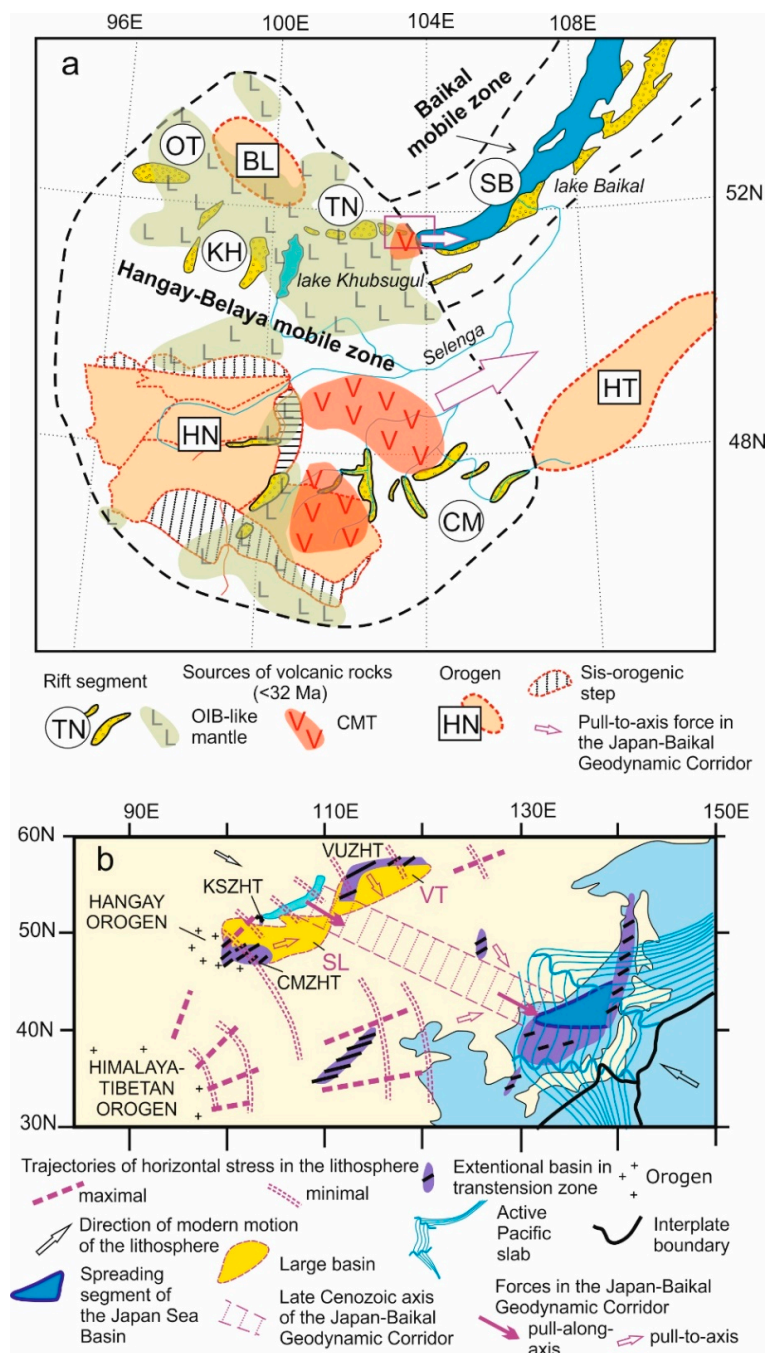


Figure 20. Transition from the “hot” (volcanic) Hangay-Belaya mobile zone of the BRS to its “cold” (non-volcanic) Baikal mobile zone (a) and spatial relationship between pull-to-axis forces in the Japan-Baikal geodynamic corridor and trajectories of tectonic stress caused by the Indo-Asian convergence (b). Panel a shows large basins (SL, Selenga) and (VT, Vitim), hot transtension zones in the central part of the BRS (KSZHT, Kamar-Stanovoy), in its southwestern part (CMZHT, Central Mongolian), and in its eastern part (VUZHT, Vitim-Udokan). Panel b shows rift segments (letters in circles: SB—South Baikal, TN—Tunka, KH—Khubsugul, OT—Oka-Todzha, CM—Central Mongolian) and orogens (letters in squares: HN—Hangay, BL—Belaya, HT—Hentey). Stress trajectories are shown after [130,131]. The pull-to-axis force of the geodynamic corridor is weakly displayed along the South Baikal Basin in magmatic activities of crust–mantle sources in the KSZHT and is more distinct in magmatic activities of crust-mantle sources of the vast area in the Selenga River basin and East Hangay Orogen in the CMZHT.

From spatial-temporal distribution of volcanism and velocity structure of the mantle, it was inferred that the lithosphere of the Baikal and Hangay-Belaya mobile zones was affected by primary melting anomalies of the transition layer (West Transbaikal and Gobi, respectively) and by secondary melting anomalies of the upper mantle (Hangay, Vitim, Udokan, and others) [18,21,132]. The Vitim and Udokan melting anomalies and those of the Sea of Japan mobile system designated quasi-periodical responses of the Japan-Baikal geodynamic corridor to 2.5 Ma great eccentricity cycles of the Earth's rotation. Similar responses recorded melting anomalies of the vast area in Eastern Sayans and Central Mongolia, synchronized with those of the Tibetan-Himalayan Orogen, as constituents of the Indo-Asian convergent region. The Tunka Valley belongs to the western "hot" (Hangay-Belaya) part of the BRS, affected by Late Cenozoic volcanism (Figure 19a), whereas the South Baikal Basin belongs to its central-northeastern "cold" (Baikal) part, which reveals melting anomalies only at the ends of the Vitim-Udokan transtension zone (Figure 20b).

From various earthquake mechanism solutions and a crustal velocity structure, we propose that the crust and sub-crustal mantle of the South Baikal Basin was attenuated due to divergent forces of the Japan-Baikal geodynamic corridor, while the crust and sub-crustal mantle of the adjacent eastern part of the Tunka Valley, on the contrary, was flattened against the rigid edge of the Siberian paleocontinent basement in connection with the development of convergent processes in the Central Asian Orogenic System. From GPS data, it was inferred that blocks of the Siberian platform and Transbaikal diverge in the South Baikal basin at the NW-SE direction (130°) at a rate of 3.4 ± 0.7 mm/year [133]. This direction of motion corresponds to the axis of the Japan-Baikal geodynamic corridor. A maximal extension of the crust results in its thinning under the Middle Baikal up to 36 km (Figure 17a). Therefore, the crust of this part of the basin is about 2 km thinner than the leveling low-crustal layer. Respectively, the low-viscosity leveling layer likely provides a dynamic link between processes of the most extended and thinned crust of the Middle Baikal and the compressed crust of the eastern end of the Tunka Valley.

Lithospheric and sub-lithospheric materials moved along the axial part of the Japan-Baikal geodynamic corridor with a maximum rate, while the rate decreased in its NNE and SSW flanks. This change created pull-to-axis forces, caused alternating volcanic impulses in the Vitim and Udokan volcanic fields of the Vitim-Udokan transtension zone [132]. Pull-to-axis forces resulted also in the almost symmetrical development of the Vitim and Selenga basins. In addition, the crust of the latter basin was affected by the Indo-Asian convergence with suppressed pull-to-axis effect of the Japan-Baikal geodynamic corridor in its upper part, but with magma generation in the deeper crust and underlying mantle.

Hot processes in the eastern end of the Tunka Valley were contemporaneous with those in the Sea of Japan mobile system. The 22–18 Ma volcanic rocks from Northeast Japan showed no systematic variations in a $^{87}\text{Sr}/^{86}\text{Sr}$ at the ocean-continent direction. Along the continental margin (from the north to the south), this isotopic ratio of volcanic rocks ranged from 0.703890–0.704195 in the Okushiri Island to 0.704874–0.705165 in the Honyo area, indicating varying proportions of asthenospheric and lithospheric components [134]. In that time, the Sea of Japan was not opened yet. Since about 18 Ma, deep-seated sources of erupted lavas indicated zoning of a dynamically linked back and frontal sides of the Northeast Japan volcanic arc. The KSZHT volcanic interval corresponded to the one of the initial subduction of the Pacific plate beneath Northeast Japan, accompanied by back-arc spreading of the crust with the Sea of Japan opening in the time interval of 18–13 Ma [135,136]. The volcanic extinction in the KSZHT coincided with the structural reorganization in the Sea of Japan mobile system caused by the collision of the Izu-Bonin and Kuril island arcs with the Northeast Japan one in the time interval of 14–12 Ma [137,138].

We infer that both in the central and in the southwestern parts of the BRS, the CMT magmatism was controlled by pull-to-axis effects in the Japan-Baikal geodynamic corridor enhanced by forces of the Indo-Asian convergence. In addition to the CMT geochemical signatures for deep-seated sources of volcanic rocks in Central Mongolia, it is noteworthy that the seismotomographic profile MOBAL-2003 [118] clearly denotes a common leveling

layer of the crust foot at a depth of about 40 km that extends from the Tunka Valley through the Orkhon-Selenga saddle to the East Hangay.

8. Conclusions

To recognize genetic links between pseudotachylytes and volcanic rocks from the central BRS, we present data on major oxides and trace elements of pseudotachylytes and host mylonites from the MSF and emphasize a magmatic origin of the former. We also characterize compositions of the MSF basic pseudotachylytes and the KSZHT volcanic rocks to show their geochemical differences from OIB that assume tectonically-derived melt generation in deep-seated sources of the Slyudyanka paleocollision zone.

Pseudotachylyte melts of basic, intermediate, and silicic compositions, injected into the Main Sayan Fault, were controlled by its junction with the Kamar-Stanovoy Zone of Hot Transtension that was active in the time interval of 18.1–11.7 Ma. From mylonite fracturing, we determine dips of these conjugated magma-controlling fault zones. We infer that the KSZHT volcanism accompanied a rift-related split off a rigid block of the Siberian paleocontinent basement along the Obruchev fault, but it became extinct when the South Baikal Basin and Tunka Valley turned out to be structurally separated from each other due to subsidence of the former and uplift of the latter.

The KSZHT volcanic rocks and the MSF basic pseudotachylytes show complementary variations of Fe, U, and alkalis in their sources occurred in the CMT and crust. From trace-element abundances of the KSZHT volcanic rocks, we distinguish garnet-bearing and garnet-free source materials and link the latter with garnet-free crystalline inclusions in lavas from the Tunka Valley. Meanwhile, lavas of the Kultuk and Meteo volcanoes erupted from both garnet-free and garnet-bearing deep-seated sources; the latter were not represented by a crystalline material. Respectively, we relate these sources to the sub-crustal garnet-bearing mantle of the CMT region. In addition, we show that lavas of the Karerny and Shirokiy volcanoes could generate in the deeper lithospheric mantle.

From uraniumogenic Pb isotope ratios of volcanic rocks, we define an initial generation of the CMT deep-seated sources of about 2.22 Ga from the Inner Asia common (deep mantle) material and its subsequent long-term evolution with distinct processing about 0.9 Ga. Comparisons between data points, distributed on the $^{208}\text{Pb}/^{204}\text{Pb}$ – $^{206}\text{Pb}/^{204}\text{Pb}$ diagram, and those, showing variations of a Th/U ratio in the KSZHT volcanic rocks, indicate a high $^{232}\text{Th}/^{238}\text{U}$ ratio in sources and their recent uranium enrichment, associated with increasing degrees of melting. No mixing of components from garnet-free and garnet-bearing sources emphasizes separate melt generations in different CMT levels during volcanic activities. We speculate that the progressively laminated CMT region could cause stricter control of melting by layers and could prevent the rising of melts, resulting in the extinction of volcanism.

To decipher a character of tectonics, responsible for the KSZHT magmatism, we use a high-resolution S-wave seismic tomography profile and interpret the CMT laminated structure of the central BRS as formed in the Neogene and Quaternary, when rift basins subsided after the Late Cretaceous and Paleogene development of the South Baikal Orogen. We suggest that vertical displacements both in the overlying rifted crust and in the underlying delaminated orogen root were compensated by lateral motions in the low-viscosity layer at the depths of 37–38 km. We explain the generation of the CMT magmatism both in the central and in the southwestern BRS as a result of cooperative pull-to-axis and convergent effects created in the Japan-Baikal Geodynamic Corridor and in the Indo-Asian interactional region, respectively. Present-day crustal deformations result in strong earthquakes distributed along the Main Sayan and Primorye sutures of the Siberian paleocontinent. Earthquake sources correspond to crustal low-velocity layers, located under the South Baikal Basin at shallower depths than under the adjacent Tunka Valley.

Supplementary Materials: The following are available online at <https://www.mdpi.com/article/10.3390/min11050487/s1>, Table S1. Analytical results on major oxides and trace elements of the standard reference materials obtained within the time interval of analyzing pseudotachylytes from

the MSF and volcanic rocks from the KSZHT, Table S2. Analytical results on major oxides and trace elements of pseudotachylytes and mylonites from the Main Sayan fault, Table S3. Analytical results on major oxides and trace elements of volcanic rocks from the KSZHT, Table S4. Analytical results on Sr, Nd, and Pb isotope ratios of volcanic rocks from the KSZHT.

Author Contributions: Conceptualization: S.R.; methodology, software: I.C., T.Y., and Y.-M.S.; validation: S.R., I.C., T.Y., E.S., N.G., Y.A.; formal analysis: S.R., I.C., and T.Y.; investigation: S.R., I.C., Y.-M.S., and Y.A.; resources: S.R.; data curation: S.R., I.C., T.Y., E.S., N.G.; writing—original draft preparation: S.R., I.C.; writing—review and editing: S.R., I.C., T.Y., and Y.-M.S.; visualization: S.R., I.C., and T.Y.; supervision: S.R. and I.C.; project administration: I.C.; funding acquisition: I.C., S.R. All authors have read and agreed to the published version of the manuscript.

Funding: This work has been funded by the RSF grant 18-77-10027.

Acknowledgments: Trace-element and isotope analyses of rocks have been performed using equipment of collective centers in Irkutsk: “Baikal Analytical Center” (Finnigan MAT mass-spectrometer, Institute of the Earth’s Crust SB RAS, analyst N.N. Fefelov), “Ultramicroanalysis” (Agilent 7500ce mass spectrometer, Limnological institute, SB RAS, analyst A.P. Chebykin), and “Isotope-Geochemical Studies” (MC-ICP-MS Neptune Plus, Vinogradov Institute of Geochemistry, SB RAS, analyst N.S. Gerasimov). Major oxides were determined by analysts G.V. Bondareva and M.M. Samoilenko (Institute of the Earth’s Crust, SB RAS). Rock magnetization in the MSF was measured by S.V. Snopkov. Photographs of thin sections were done by S.A. Sasim. We are grateful to all colleagues assisted in this work. Additionally, we thank V. Mordvinova presented a color version of the S-wave profile and also two reviewers for thoughtful comments.

Conflicts of Interest: The authors declare no conflict of interest.

References

- Hirano, N.; Takahashi, E.; Yamamoto, J.; Abe, N.; Ingle, S.P.; Kaneoka, I.; Hirata, T.; Kimura, J.-I.; Ishii, T.; Ogawa, Y.; et al. Volcanism in response to plate flexure. *Science* **2006**, *313*, 1426–1428. [[CrossRef](#)] [[PubMed](#)]
- Coltice, N.; Bertrand, H.; Rey, P.; Jourdan, F.; Phillips, B.R.; Ricard, Y. Global warming of the mantle beneath continents back to the Archaean. *Gondwana Res.* **2009**, *15*, 254–266. [[CrossRef](#)]
- Lipman, P.W. Alkalic and tholeiitic basaltic volcanism related to the Rio Grande basin. *Geol. Soc. Am. Bull.* **1969**, *80*, 1343–1354. [[CrossRef](#)]
- Lipman, P.W. Incremental assembly and prolonged consolidation of Cordilleran magma chambers: Evidence from the Southern Rocky Mountain volcanic field. *Geosphere* **2007**, *3*, 42–70. [[CrossRef](#)]
- Dungan, M.A.; Thompson, R.A.; Stormer, J.S.; Neill, J.M. Rio Grande Rift volcanism: Northeastern Jemez Zone, New Mexico. In *Field Excursions to Volcanic Terranes in the Western United States. V. 1. Southern Rocky Mountain Region*; New Mexico Bureau of Mines & Mineral Resources: Socorro, Brazil, 1989; pp. 435–486.
- Duncker, K.E.; Wolff, J.A.; Harmon, R.S.; Leat, P.T.; Dickin, A.P.; Thompson, R.N. Diverse mantle and crustal components in lavas of the NW Cerros Del Rio volcanic field, Rio Grande Rift, New Mexico. *Contrib. Miner. Pet.* **1991**, *108*, 331–345. [[CrossRef](#)]
- Asmerom, Y. Th-U fractionation and mantle structure. *Earth Planet. Sci. Lett.* **1999**, *166*, 163–175. [[CrossRef](#)]
- McMillan, N.J.; Dickin, A.P.; Haag, D. Evolution of Magma Source Regions in the Rio Grande Rift, Southern New Mexico. *Geology* **2000**, *112*, 1582–1593. [[CrossRef](#)]
- Rasskazov, S.V.; Saranina, E.V.; Martynov, Yu.A.; Chashchin, A.A.; Maksimov, S.O.; Brandt, I.S.; Brandt, S.B.; Maslovskaya, M.N.; Kovalenko, S.V. Evolution of Late Cenozoic magmatism in the active continental margin of Southern Primorye. *Russ. J. Pac. Geol.* **2003**, *1*, 92–109. (In Russian)
- Rasskazov, S.V.; Brandt, S.B.; Brandt, I.S. *Radiogenic Isotopes in Geologic Processes*; Springer: Berlin/Heidelberg, Germany, 2010. [[CrossRef](#)]
- Rasskazov, S.; Sun, Y.-M.; Chuvashova, I.; Yasnygina, T.; Yang, C.; Xie, Z.; Saranina, E.; Gerasimov, N.; Vladimirova, T. Trace-Element and Pb isotope evidence on extracting sulfides from potassic melts beneath Longmenshan and Molabushan volcanoes, Wudalianchi, Northeast China. *Minerals* **2020**, *10*, 319. [[CrossRef](#)]
- Lustrino, M.; Carminati, E. Phantom plumes in Europe and the circum-Mediterranean region. In *Plates, Plumes, and Planetary Processes: Geological Society of America Special Paper*; Foulger, G.R., Jurdy, D.M., Eds.; 2007; Volume 430, pp. 723–745. [[CrossRef](#)]
- Lustrino, M.; Wilson, M. The circum-Mediterranean anorogenic Cenozoic igneous province. *Earth-Sci. Rev.* **2007**, *81*, 1–65. [[CrossRef](#)]
- Corti, G. Continental rift evolution: From rift initiation to incipient break-up in the Main Ethiopian Rift, East Africa. *Earth-Sci. Rev.* **2009**, *96*, 1–53. [[CrossRef](#)]
- Seghedi, I.; Ersoy, Y.E.; Helvac, C. Miocene—Quaternary volcanism and geodynamic evolution in the Pannonian Basin and the Menderes Massif: A comparative study. *Lithos* **2013**, *180–181*, 25–42. [[CrossRef](#)]

16. Rooney, T.O.; Nelson, W.R.; Dosso, L.; Furman, T.; Hanan, B. The role of continental lithosphere metasomes in the production of HIMU-like magmatism on the northeast African and Arabian plates. *Geology* **2014**, *42*, 419–422. [[CrossRef](#)]
17. Accardo, N.J.; Gaherty, J.B.; Shillington, D.J.; Hopper, E.; Nyblade, A.A.; Ebinger, C.J.; Scholz, C.A.; Chindandali, P.R.N.; Wambura-Ferdinand, R.; Mbogoni, G.; et al. Thermochemical modification of the upper mantle beneath the northern Malawi Rift constrained from shear velocity imaging. *Geochem. Geophys. Geosyst.* **2020**, *21*, e2019GC008843. [[CrossRef](#)]
18. Rasskazov, S.V.; Chuvashova, I.S. The latest geodynamics in Asia: Synthesis of data on volcanic evolution, lithosphere motion, and mantle velocities in the Baikal-Mongolian region. *Geosci. Front.* **2017**, *8*, 733–752. [[CrossRef](#)]
19. Rasskazov, S.V.; Chuvashova, I.S.; Yasnygina, T.A.; Fefelov, N.N.; Saranina, E.V. *Potassic and Potassic-Sodic Volcanic Series in the Cenozoic of Asia*; Academic Publishing House “GEO”: Novosibirsk, Russia, 2012. (In Russian)
20. Rasskazov, S.V.; Yasnygina, T.A.; Chuvashova, I.S.; Mikheeva, E.A.; Snopkov, S.V. The Kultuk Volcano: Spatial-Temporal change of magmatic sources at the western terminus of the South Baikal Basin between 18 and 12 Ma. *Geodyn. Tectonophys.* **2013**, *4*, 135–168. [[CrossRef](#)]
21. Chuvashova, I.; Rasskazov, S.; Yasnygina, T. Mid-Miocene thermal impact on the lithosphere by sub-lithospheric convective mantle material: Transition from high- to moderate-Mg magmatism beneath Vitim Plateau, Siberia. *Geosci. Front.* **2017**, *8*, 753–774. [[CrossRef](#)]
22. Sibson, R.H. Generation of pseudotachylyte by ancient seismic faulting. *Geophys. J. Int.* **1975**, *43*, 775–794. [[CrossRef](#)]
23. Sibson, R.H. Fault rocks and fault mechanisms. *J. Geol. Soc. Lond.* **1977**, *133*, 191–213. [[CrossRef](#)]
24. Cowan, D.S. Do faults preserve a record of seismic slip? A field geologist’s opinion. *J. Struct. Geol.* **1999**, *21*, 995–1001. [[CrossRef](#)]
25. Swanson, M.T. Fault structure, wear mechanisms and rupture processes in pseudotachylyte generation. *Tectonophysics* **1992**, *204*, 223–242. [[CrossRef](#)]
26. Swanson, M.T. Geometry and kinematics of adhesive wear in brittle strike-slip fault zones. *J. Struct. Geol.* **2005**, *27*, 871–887. [[CrossRef](#)]
27. Passchier, C.W. Pseudotachylyte and the development of ultramylonite bands in the Saint-Barthelemy Massif, French Pyrenees. *J. Struct. Geol.* **1982**, *4*, 69–79. [[CrossRef](#)]
28. Hobbs, B.E.; Ord, A.; Teyssier, C. Earthquakes in the ductile regime. *Pure Appl. Geophys.* **1986**, *124*, 309–336. [[CrossRef](#)]
29. White, J.C. Transient discontinuities revisited: Pseudotachylyte, plastic instability and the influence of low pore fluid pressure on deformation processes in the mid-crust. *J. Struct. Geol.* **1986**, *18*, 1471–1486. [[CrossRef](#)]
30. Pennacchioni, G.; Cesare, B. Ductile-Brittle transition in pre-Alpine amphibolite facies mylonites during evolution from water-present to water-deficient conditions (Mont Mary nappe, Italian Western Alps). *J. Metamorph. Geol.* **1997**, *15*, 777–791. [[CrossRef](#)]
31. Magloughlin, J.F. Microstructural and chemical changes associated with cataclasis and frictional melting at shallow crustal levels: The cataclasite pseudotachylyte connection. *Tectonophysics* **1992**, *204*, 243–260. [[CrossRef](#)]
32. Sarkar, A.; Chattopadhyay, A. Microstructure and geochemistry of pseudotachylyte veins from Sarwar-Junia Fault Zone, India: Implications for frictional melting process in a seismic fault zone. *Geol. J.* **2020**, 1–29. [[CrossRef](#)]
33. Clerc, A.; Renard, F.; Austrheim, H.; Jamtveit, B. Spatial and size distributions of garnets grown in a pseudotachylyte generated during a lower crust earthquake. *Tectonophysics* **2018**, *733*, 159–170. [[CrossRef](#)]
34. Wang, H.; Li, H.; Si, J.; Zhang, L.; Sun, Z. Geochemical features of the pseudotachylytes in the Longmen Shan thrust belt, eastern Tibet. *Quat. Int.* **2019**, *514*, 173–185. [[CrossRef](#)]
35. Orlandini, O.; Mahan, K.H. Rheological evolution of a pseudotachylyte-bearing deep crustal shear zone in the western Canadian shield. *J. Struct. Geol.* **2020**, *141*, 104188. [[CrossRef](#)]
36. Shand, S.J. The pseudotachylyte of Parijs (Orange Free State), and its relation to Trap-Shotten Gneiss ‘and Flinty Crush-Rock’. *Q. J. Geol. Soc.* **1916**, *72*, 198–221. [[CrossRef](#)]
37. Philpotts, A.R. Origin of pseudotachylytes. *Am. J. Sci.* **1964**, *262*, 1008–1035. [[CrossRef](#)]
38. Allen, J.L. A multi-kilometer pseudotachylyte system as an exhumed record of earthquake rupture geometry at hypocentral depths (Colorado, USA). *Tectonophysics* **2005**, *402*, 37–54. [[CrossRef](#)]
39. Bossiere, G. Petrology of pseudotachylytes from the Alpine Fault of New Zealand. *Tectonophysics* **1991**, *196*, 173–193. [[CrossRef](#)]
40. Maddock, R.H. Effects of lithology, cataclasis and melting on the composition of fault-generated pseudotachylytes in Lewisian gneiss, Scotland. *Tectonophysics* **1992**, *204*, 261–278. [[CrossRef](#)]
41. Lin, A. *Fossil Earthquakes: The Formation and Preservation of Pseudotachylytes (Volume 111)*; Springer: Heidelberg/Berlin, Germany, 2007. [[CrossRef](#)]
42. Maddock, R.H. Melt origin of fault-generated pseudotachylytes demonstrated by textures. *Geology* **1983**, *11*, 105–108. [[CrossRef](#)]
43. Spray, J.G. Pseudotachylyte controversy: Fact or fiction? *Geology* **1995**, *23*, 1119–1122. [[CrossRef](#)]
44. Lin, A. Injection veins of crushing-originated pseudotachylyte and fault gouge formed during seismic faulting. *Eng. Geol.* **1996**, *43*, 213–224. [[CrossRef](#)]
45. Lin, A.; Shimamoto, T. Selective melting processes as inferred from experimentally generated pseudotachylytes. *J. Asian Earth Sci.* **1998**, *16*, 533–545. [[CrossRef](#)]
46. Tsutsumi, A. Size distribution of clasts in experimentally produced pseudotachylytes. *J. Struct. Geol.* **1999**, *21*, 305–312. [[CrossRef](#)]
47. Ozawa, K.; Takizawa, S. Amorphous material formed by the mechanochemical effect in natural pseudotachylyte of crushing origin: A case study of the Iida-Matsukawa Fault, Nagano Prefecture, Central Japan. *J. Struct. Geol.* **2007**, *29*, 1855–1869. [[CrossRef](#)]

48. O'Hara, K. Major-and trace-element constraints on the petrogenesis of a fault-related pseudotachylyte, western Blue Ridge Province, North Carolina. *Tectonophysics* **1992**, *204*, 279–288. [[CrossRef](#)]
49. Spray, J.G. Artificial generation of pseudotachylyte using friction welding apparatus: Simulation of melting on a fault plane. *J. Struct. Geol.* **1987**, *9*, 49–60. [[CrossRef](#)]
50. Sibson, R.H. Interactions between temperature and pore fluid pressure during an earthquake faulting and a mechanism for partial or total stress relief. *Nature* **1973**, *243*, 66–68. [[CrossRef](#)]
51. Rempel, A.W.; Rice, J.R. Thermal pressurization and onset of melting in fault zone. *J. Geophys. Res.* **2006**, *111*, B09314. [[CrossRef](#)]
52. Ruzhich, V.V.; Kocharyan, G.G.; Savelieva, V.B.; Travin, A.V. On the structure and formation of earthquake sources in the faults located in the subsurface and deep levels of the crust. Part II. Deep level. *Geodyn. Tectonophys.* **2018**, *9*, 1039–1061. [[CrossRef](#)]
53. Zamaraev, S.M.; Mazukabzov, A.M.; Ryazanov, G.V.; Sezko, A.I.; Vasiliev, E.P.; Grabkin, O.V. *Old Structure of the Earth's Crust in Eastern Siberia*; Publishing House "Science". Sib. Department: Novosibirsk, Russia, 1975. (In Russian)
54. Zamarayev, S.M.; Vasilyev, E.P.; Mazukabzov, A.M.; Ruzhich, V.V. *The Relationship between Ancient and Cenozoic Structures in the Baikal Rift Zone*; Nauka, Siberian Branch: Novosibirsk, Russia, 1979. (In Russian)
55. Rasskazov, S.; Ilyasova, A.; Bornyakov, S.; Chuvashova, I.; Chebykin, E. Responses of a $^{234}\text{U}/^{238}\text{U}$ activity ratio in groundwater to earthquakes in the South Baikal Basin, Siberia. *Front. Earth Sci.* **2020**. [[CrossRef](#)]
56. Seminsky, K.Zh.; Bornyakov, S.A.; Dobrynina, A.A.; Radziminovich, N.A.; Rasskazov, S.V.; Sankov, V.A.; Mialle, P.; Bobrov, A.A.; Ilyasova, A.M.; Salko, D.V.; et al. The Bystrinskoe earthquake in the southern Baikal region (21 September 2020, Mw = 5.4): Main parameters, precursors, and accompanying effects. *Russ. Geol. Geophys.* **2021**, *62*. (In press)
57. Rasskazov, S.V. *Magmatism of the Baikal Rift System*; Siberian Publishing Company Science: Novosibirsk, Russia, 1993. (In Russian)
58. Ionov, D.A.; O'Reilly, S.Y.; Ashchepkov, I.V. Feldspar-Bearing lherzolite xenoliths in alkali basalts from Hamar-Daban, southern Baikal region, Russia. *Contrib. Miner. Pet.* **1995**, *122*, 174–190. [[CrossRef](#)]
59. Ashchepkov, I.V.; Travin, A.V.; Saprykin, A.I.; Andre, L.; Gerasimov, P.A.; Khmelnikova, O.S. Age of xenolith-bearing basalts and mantle evolution in the Baikal rift zone. *Russ. Geol. Geophys.* **2003**, *44*, 1121–1149.
60. Ailow, Y.; Rasskazov, S.V.; Chuvashova, I.S.; Yasnygina, T.A. Relationship between rocks of primitive mantle, restites, and metasomatites in inclusions from basanites of the Karerny Volcano (Western Pribaikal). *Bull. Irkutsk State Univ. Ser. Earth Sci.* **2019**, *29*, 3–23. [[CrossRef](#)]
61. Danilovich, V.N. *Fundamentals of Deformation Theory of Geological Bodies*; Irkut. Book Publishing House: Irkutsk, Russia, 1953. (In Russian)
62. Sizykh, Y.I. *A Comprehensive Scheme for the Chemical Analysis of Rocks and Minerals. Open-File Report*; Institute of the Earth's Crust SB AS USSR: Irkutsk, Russia, 1985. (In Russian)
63. Faure, G. *Origin of Igneous Rocks: The Isotopic Evidence*; Springer: Berlin/Heidelberg, Germany, 2001.
64. Yasnygina, T.A.; Markova, M.E.; Rasskazov, S.V.; Pakhomova, N.N. Determination of rare earth elements, Y, Zr, Nb, Hf, Ta, and Th in geological reference materials of the DV series by ICP-MS. *Zavod. Lab. Diagn. Mater.* **2015**, *81*, 10–20. (In Russian)
65. Belichenko, V.G.; Reznitsky, L.Z.; Makrygina, V.A.; Barash, I.G. Terranes of the Baikal-Khubsugul fragment of the Central Asian mobile belt of Paleozooids. The state of the problem. In *Geodynamic Evolution of the Lithosphere in the Central Asian Mobile Belt (from the Ocean to the Continent)*; Institute of the Earth's Crust SB RAS: Irkutsk, Russia, 2006; Volume 1, pp. 37–40. (In Russian)
66. Zamaraev, S.M.; Sizykh, V.I.; Meshalkin, S.I.; Novokshonov, Y.A. Structural features of the Angara thrust. *Geol. Geophys.* **1983**, *5*, 126–129. (In Russian)
67. Chuvashova, I.S.; Hassan, A.; Al Hamud, A.; Kovalenko, S.N.; Rudneva, N.A.; Rasskazov, S.V. Transition from the Selenga-Vitim foredeep to the Vitim plateau: Cenozoic sedimentation and volcanism. *Bull. Irkutsk State Univ. Earth Sci. Ser.* **2019**, *27*, 138–153. [[CrossRef](#)]
68. Logatchev, N.A. Sayan-Baikal and Stanovoy highlands. In *Highlands of Pribaikal and Transbaikali*; Nauka, Moscow, 1974. (In Russian)
69. Logatchev, N.A.; Zorin, Yu.A. Baikal Rift Zone: Structure and geodynamics. *Tectonophysics* **1992**, *208*, 273–286. [[CrossRef](#)]
70. Hutchinson, D.R.; Golmshtok, A.J.; Zonenshain, L.P.; Moore, T.C.; Scholz, C.A.; Klitgord, K.D. Depositional and tectonic framework of the rift basins of Lake Baikal from multichannel seismic data. *Geology* **1992**, *20*, 589–592. [[CrossRef](#)]
71. Sherman, S.I. Faults of the Baikal rift zone. *Tectonophysics* **1978**, *45*, 31–39. [[CrossRef](#)]
72. Sherman, S.I. Faults and tectonic stresses of the Baikal rift zone. *Tectonophysics* **1992**, *208*, 297–307. [[CrossRef](#)]
73. Shafeev, A.A. *The Precambrian of the South-Western Baikal and Khamar-Daban*; Nauka: Moscow, Russia, 1970. (In Russian)
74. Vasil'ev, E.P.; Reznitsky, L.Z.; Vishnyakov, V.N.; Nekrasova, E.A. *The Slyudyanka Crystalline Complex*; Nauka: Novosibirsk, Russia, 1981. (In Russian)
75. Le Bas, M.J.; Streckeisen, A.L. The IUGS systematics of igneous rocks. *J. Geol. Soc. Lond.* **1991**, *148*, 825–833. [[CrossRef](#)]
76. Stepanov, L.V.; Lipenkov, G.V.; Lokhov, K.I.; Saltykova, T.E. Isotope-Geochemical substantiation of the age of carbonate rocks of the Slyudyanka crystalline complex. *Reg. Geol. Metallog.* **2011**, *48*, 60–68. (In Russian)
77. McDonough, W.F.; Sun, S.-S. The composition of the Earth. *Chem. Geol.* **1995**, *120*, 223–253. [[CrossRef](#)]
78. Kutolin, V.A. On the order and temperatures of crystallization of minerals in rocks of basic composition. *Russ. Geol. Geophys.* **1966**, *11*, 42–51. (In Russian)
79. Arndt, N.; Lesher, C.M.; Barnes, S.J. *Komatiite*; Cambridge University Press: Cambridge, UK, 2008.
80. Herzberg, C.; Asimov, N.; Arndt, N.; Niu, Y.; Lesher, C.M.; Fitton, J.G.; Cheadle, M.J.; Saunders, A.D. Temperatures in ambient mantle and plumes: Constraints from basalts, picrites, and komatiites. *Geochem. Geophys. Geosyst.* **2007**, *8*, Q02006. [[CrossRef](#)]

81. Hirose, K.; Kushiro, I. Partial melting of dry peridotites at high pressure: Determination of compositions of melts segregated from peridotite using aggregates of diamond. *Earth Planet. Sci. Lett.* **1993**, *114*, 477–489. [[CrossRef](#)]
82. O'Reilly, S.Y.; Griffin, W.L. 4-D lithosphere mapping: Methodology and examples. *Tectonophysics* **1996**, *262*, 3–18. [[CrossRef](#)]
83. Shaw, D.M. Trace element fractionation during anatexis. *Geochim. Cosmochim. Acta* **1970**, *34*, 237–243. [[CrossRef](#)]
84. Chuvashova, I.S.; Rasskazov, S.V.; Yasnygina, T.A.; Mikheeva, E.A. High-Mg lavas from the Dariganga volcanic field in the south-eastern Mongolia: Petrogenetic model of magmatism at the asthenosphere–lithosphere boundary. *Geodyn. Tectonophys.* **2012**, *3*, 385–407. [[CrossRef](#)]
85. Hofmann, A.W.; Jochum, K.P.; Seufert, M.; White, W.M. Nb and Pb in oceanic basalts: New constraints on mantle evolution. *Earth Planet. Sci. Lett.* **1986**, *79*, 33–45. [[CrossRef](#)]
86. Miller, D.M.; Goldstein, S.L.; Langmuir, C.H. Cerium/lead and lead isotope ratios in arc magmas and the enrichment of lead in the continents. *Nature* **1994**, *368*, 514–519. [[CrossRef](#)]
87. Pearce, J.A. Role of the sub-continental lithosphere in magma genesis at active continental margins. In *Continental Basalts and Mantle Xenoliths*; Hawkesworth, C.L., Norry, M.J., Eds.; Shiva: Nantwich, UK, 1983; pp. 230–249.
88. Sun, S.-S.; McDonough, W.F. Chemical and isotopic systematics of oceanic basalts: Implications for mantle composition and processes. In *Magmatism in the Ocean Basins. Geological Society Special Publication*; Saunders, A.D., Norry, M.J., Eds.; Geological Society Publishing House: Bath, UK, 1989; Volume 42, pp. 313–345. [[CrossRef](#)]
89. Rudnick, R.L.; Fountain, D.M. Nature and composition of the continental crust: A lower crustal perspective. *Rev. Geophys.* **1995**, *33*, 267–309. [[CrossRef](#)]
90. Steiger, R.H.; Jäger, E. Subcommittee on geochronology: Convention on the use of decay constants in geo- and cosmology. *Earth Planet. Sci. Lett.* **1977**, *36*, 359–362. [[CrossRef](#)]
91. Hofmann, A.W. Nb in Hawaiian magmas: Constraints on source composition and evolution. *Chem. Geol.* **1986**, *57*, 17–30. [[CrossRef](#)]
92. Beattie, P. Uranium–Thorium disequilibria and partitioning on melting of garnet peridotite. *Nature* **1993**, *363*, 63–65. [[CrossRef](#)]
93. Foley, S.F.; Petibon, C.M. High U/Th partitioning by clinopyroxene from alkali silicate and carbonatite metasomatism: An origin for Th/U disequilibrium in mantle melts? *Terra Nova* **2001**, *13*, 104–109. [[CrossRef](#)]
94. Rasskazov, S.; Chuvashova, I.; Yasnygina, T.; Saranina, E. Mantle evolution of Asia inferred from Pb isotopic signatures of sources for Late Phanerozoic volcanic rocks. *Minerals* **2020**, *10*, 739. [[CrossRef](#)]
95. Hart, S.R. A large-scale isotope anomaly in the Southern Hemisphere mantle. *Nature* **1984**, *309*, 753–757. [[CrossRef](#)]
96. Turkina, O.M.; Urmantseva, L.N.; Berezhnaya, N.G.; Presnyakov, S.L. Paleoproterozoic age of the protoliths of metaterigenous rocks in the east of the Irkut granulite-gneiss block (Sharyzhalgai salient, Siberian Craton). *Strat. Geol. Correl.* **2010**, *18*, 16–30. [[CrossRef](#)]
97. Salnikova, E.B.; Kotov, A.B.; Levitskii, V.I.; Reznitskii, L.Z.; Mel'nikov, A.I.; Kozakov, I.K.; Kovach, V.P.; Barash, I.G.; Yakovleva, S.Z. Age constraints of high-temperature metamorphic events in crystalline complexes of the Irkut block, the Sharyzhalgai ledge of the Siberian platform basement: Results of the U–Pb single zircon dating. *Strat. Geol. Correl.* **2007**, *15*, 343–358. [[CrossRef](#)]
98. Levitsky, V.I. *Petrology and Geochemistry of Metasomatism during the Formation of the Continental Crust*; Academic Publishing House “Geo”: Novosibirsk, Russia, 2005. (In Russian)
99. Grudin, M.I.; Menshagin, Y.V. *Ultramafic–Basic Associations of the Early Precambrian*; Nauka: Novosibirsk, Russia, 1987. (In Russian)
100. Aftalion, M.; Bibikova, E.V.; Bowes, D.R.; Hopgood, A.M.; Perchuk, L.L. Timing of Early Proterozoic collisional and extensional events in the granulite-gneiss-charnokite-granite complex, lake Baikal, USSR: A U–Pb, Rb–Sr and Sm–Nd isotopic study. *J. Geol.* **1991**, *99*, 851–861. [[CrossRef](#)]
101. Didenko, A.N.; Kozakov, I.K.; Bibikova, E.V.; Vodovozov, V.Y.; Khil'tova, V.Ya.; Reznitskii, L.S.; Ivanov, A.V.; Levitskii, V.I.; Travin, A.V.; Shevchenko, D.O.; et al. Paleoproterozoic granites of the Sharyzhalgai block, Siberian craton: Paleomagnetism and geodynamic inferences. *Dokl. Earth Sci.* **2003**, *390*, 510–515.
102. Rozen, O.M.; Manakov, A.V.; Zinchuk, N.N. *Siberian Craton: Origin and the Diamond Control*; Scientific World: Moscow, Russia, 2006. (In Russian)
103. Donskaya, T.V. Assembly of the Siberian Craton: Constraints from Paleoproterozoic granitoids. *Precambrian Res.* **2020**, *348*, 105869. [[CrossRef](#)]
104. Vladimirov, B.M.; Logatchev, N.A.; Weiner-Krotova, G.A.; Lepin, V.S.; Ivanov, A.V.; Rasskazov, S.V. The Vendian–Cambrian boundary: Rb–Sr–Isochron age of the final event of alkaline-ultrabasic magmatism in the northeastern Sayan region. *Dokl. Earth Sci.* **2003**, *389*, 346–349.
105. Ashchepkov, I.; Zhmodik, S.; Belyanin, D.; Kiseleva, O.N.; Medvedev, N.; Travin, A.; Yudin, D.; Karmanov, N.S.; Downes, H. Aillikites and Alkali Ultramafic Lamprophyres of the Beloziminsky Alkaline Ultrabasic–Carbonatite Massif: Possible Origin and Relations with Ore Deposits. *Minerals* **2020**, *10*, 404. [[CrossRef](#)]
106. Salnikova, E.B.; Sergeev, S.A.; Kotov, A.B.; Yakovleva, S.Z.; Steiger, R.H.; Reznitskiy, L.Z.; Vasil'ev, E.P. U–Pb zircon dating of granulite metamorphism in the Sludyanskiy complex, Eastern Siberia. *Gondwana Res.* **1998**, *1*, 195–205. [[CrossRef](#)]
107. Levitsky, V.I.; Plyusnin, G.S. New data on petrology, geochemistry and geochronology of the Bystraya massif. *Russ. Geol. Geophys.* **1991**, *2*, 22–28. (In Russian)

108. Grudin, M.I.; Rasskazov, S.V.; Kovalenko, S.N.; Ilyasova, A.M. Early Paleozoic Snezhnaya gabbro-syenite intrusion in South-western Baikal Region (trace-element signature of crust/mantle mixing). *Russ. Geol. Geophys.* **2004**, *45*, 1043–1052.
109. Amirzhanov, A.A. Fundamental problem of the relationship between ore genesis and trap magmatism on the Siberian platform. In *New and Non-Traditional Types of Mineral Deposits in the Baikal and Transbaikalia, Proceedings of All-Russia Scientific-Practical Conference*; Geological Institute SB RAS: Ulan-Ude, Russia, 6 October 2010; pp. 18–21. (In Russian)
110. Bulnaev, K.B. On the carbonatite nature of endogenous carbonate rocks of Transbaikalia. *Dokl. Earth Sci.* **1997**, *354*, 653–656. (In Russian)
111. Yarmolyuk, V.V.; Kovalenko, V.I.; Ivanov, V.G.; Vladykin, N.V.; Nikiforov, A.V.; Ripp, G.S. Late Mesozoic volcanic carbonatites from the Transbaikalia region. *Dokl. Earth Sci.* **1997**, *355*, 845–849.
112. Rasskazov, S.V.; Chuvashova, I.S.; Mikolaichuk, A.V.; Sobel, E.P.; Yasnygina, T.A.; Fefelov, N.N.; Saranina, E.V. Lateral change of sources for Cretaceous–Paleogene magmatism in the Tian-Shan. *Petrology* **2015**, *23*, 281–308. [[CrossRef](#)]
113. Zorin, Y.A.; Novoselova, M.R.; Turutanov, E.Kh.; Kozhevnikov, V.M. The structure of the lithosphere of the Mongolian–Siberian mountainous terrane. In *Geodynamics of Inland Mountainous Regions*; Science. Sib. Department: Novosibirsk, Russia, 1990; pp. 143–154. (In Russian)
114. Melnikova, V.I.; Gileva, N.A.; Arefiev, S.S.; Bykova, V.V.; Masalskiy, O.K. The 27 August 2008, $M_w = 6.3$ Kultuk earthquake (South Baikal): The stress-strain state of the source area from the aftershock data. *Izv. Phys. Solid Earth* **2013**, *49*, 563–576. [[CrossRef](#)]
115. Mats, V.D.; Ufimtsev, G.F.; Mandelbaum, M.M.; Alakshin, A.M.; Pospeev, A.B.; Shimaraev, M.N.; Khlystov, O.M. *The Cenozoic Baikal Rift Basin: Its Structure and Geological History*; Geo Branch, Publishing House of SB RAS: Novosibirsk, Russia, 2001. (In Russian)
116. Mordvinova, V.V.; Kobleev, M.M.; Khritova, M.A.; Turutanov, E.Kh.; Kobleeva, E.A.; Trynkova, D.S.; Tsydypova, L.R. The deep velocity structure of the southern margin of the Siberian Craton with respect to Baikal rifting. *Dokl. Earth Sci.* **2019**, *484*, 66–70. [[CrossRef](#)]
117. Krylov, S.V.; Mandelbaum, M.M.; Mishen'kin, B.P.; Mishen'kina, Z.R.; Petrik, G.V.; Seleznev, V.S. *The Earth's Interior Beneath Baikal from Seismic Data*; Nauka Publisher: Novosibirsk, Russia, 1981. (In Russian)
118. Mordvinova, V.V.; Deschamps, A.; Dugarmaa, T.; Deverchère, J.; Ulziibat, M.; Sankov, V.A.; Artem'ev, A.A.; Perrot, J. Velocity Structure of the Lithosphere on the 2003 Mongolian Baikal Transect from SV Waves. *Izv. Phys. Solid Earth* **2007**, *43*, 119–129. [[CrossRef](#)]
119. Mordvinova, V.V.; Artemyev, A.A. The three-dimensional shear velocity structure of lithosphere in the southern Baikal Rift System and its surroundings. *Russ. Geol. Geophys.* **2010**, *51*, 694–707. [[CrossRef](#)]
120. Zamaraev, S.M.; Samsonov, V.V. Geological structure and oil and gas content of the Selenga depression. In *Geology and Oil and Gas Potential of Eastern Siberia*; Gospotekhizdat: Moscow, Russia, 1959; pp. 465–474. (In Russian)
121. Al Hamoud, A.; Rasskazov, S.V.; Chuvashova, I.S.; Tregub, T.F.; Rubtsova, M.N.; Kolomiyets, V.L.; Budaev, R.Ts.; Hassan, A.; Volkov, M.A. Overturned Eocene–Lower Pliocene alluvial stratum on the southern coast of Lake Baikal and its neotectonic significance. *Geodyn. Tectonophys.* **2021**, *12*, 139–156. [[CrossRef](#)]
122. Watanabe, T.; Koyaguchi, T.; Seno, T. Tectonic stress controls on ascent and emplacement of magmas. *J. Volcanol. Geotherm. Res.* **1999**, *91*, 65–78. [[CrossRef](#)]
123. Suvorov, V.D.; Mishen'kina, Z.P. Structure of sedimentary cover and basement beneath the South Basin of Lake Baikal inferred from seismic profiling. *Russ. Geol. Geophys.* **2005**, *46*, 1141–1149. [[CrossRef](#)]
124. Kontorovich, A.E.; Kashirtsev, V.A.; Moskvina, V.I.; Burshtein, L.M.; Zemskaia, T.I.; Kostyreva, E.A.; Kalmychkov, G.V.; Khlystov, O.M. Petroleum potential of sediments of Lake Baikal. *Russ. Geol. Geophys.* **2007**, *48*, 1046–1053. [[CrossRef](#)]
125. Berzin, N.A. *Zone of the Main Fault in Eastern Sayans*; Nauka: Moscow, Russia, 1967. (In Russian)
126. Parfenov, L.M. *The Main Features of the Precambrian Structure of the Eastern Sayan*; Nauka: Moscow, Russia, 1967. (In Russian)
127. HRVD. Department of Geological Sciences, Harvard University, 20 Oxford St., Cambridge, MA 02138, U.S.A. Available online: <http://www.seismology.harvard.edu/> (accessed on 1 April 2021).
128. Radziminovich, N.A.; Melnikova, V.I.; San'kov, V.A.; Levi, K.G. Seismicity and seismotectonic deformations of the crust in the Southern Baikal basin. *Izv. Phys. Solid Earth* **2006**, *42*, 904–920. [[CrossRef](#)]
129. Seredkina, A.I.; Melnikova, V.I. Seismic moment tensor of Pribaikalye earthquakes from the surface-wave amplitude spectra. *Izv. Phys. Solid Earth* **2014**, *50*, 403–414. [[CrossRef](#)]
130. Sankov, V.A.; Parfeevets, A.V.; Lukhnev, A.V.; Miroshnichenko, A.I.; Ashurkov, S.V. Late Cenozoic geodynamics and mechanical coupling of crustal and upper mantle deformations in the Mongolia–Siberia mobile area. *Geotectonics* **2011**, *45*, 378–393. [[CrossRef](#)]
131. Xu, Z.; Wang, S.; Huang, Y.; Gao, A. Tectonic stress field of China inferred from a large number of small earthquakes. *J. Geophys. Res.* **1992**, 11867–11877. [[CrossRef](#)]
132. Chuvashova, I.; Rasskazov, S.; Sun, Y.; Yang, C. Origin of melting anomalies in the Japan–Baikal corridor of Asia at the latest geodynamic stage: Evolution from the mantle transition layer and generation by lithospheric transtension. *Geodyn. Tectonophys.* **2017**, *8*, 435–440. [[CrossRef](#)]
133. Sankov, V.A.; Lukhnev, A.V.; Miroshnichenko, A.I.; Dobrynin, A.A.; Ashurkov, S.V.; Byzov, L.M.; Dembelov, M.G.; Calais, E.; Deversher, J. Contemporary Horizontal Movements and Seismicity of the South Baikal Basin (Baikal Rift System). *Izv. Phys. Solid Earth* **2014**, *50*, 785–794. [[CrossRef](#)]

134. Sato, M.; Shuto, K.; Yagi, M. Mixing of asthenospheric and lithospheric mantle-derived basalt magmas as shown by along-arc variation in Sr and Nd isotopic compositions of Early Miocene basalts from back-arc margin of the NE Japan arc. *Lithos* **2007**, *96*, 453–474. [[CrossRef](#)]
135. Shuto, K.; Ohki, J.; Kagami, H.; Yamamoto, M.; Watanabe, N.; Yamamoto, K.; Anzai, N.; Itaya, T. The relationships between drastic changes in Sr isotope ratios of magma sources beneath the NE Japan arc and the spreading of the Japan Sea back-arc basin. *Miner. Pet.* **1993**, *49*, 71–90. [[CrossRef](#)]
136. Otofujii, Y.-I. Large tectonic motion of the Japan Arc in late Cenozoic times inferred from paleomagnetism: Review and synthesis. *Isl. Arc* **1996**, *5*, 229–249. [[CrossRef](#)]
137. Jolivet, L.; Tamaki, K.; Fournier, M. Japan Sea opening history and mechanism: A synthesis. *J. Geophys. Res.* **1994**, *99*, 22237–22259. [[CrossRef](#)]
138. Kusunoki, K.; Kimura, G. Collision and extrusion at the Kuril–Japan junction. *Tectonics* **1998**, *17*, 843–858. [[CrossRef](#)]